

# Solar-induced fluorescence products show variable skill in constraining global patterns in biospheric CO<sub>2</sub> fluxes

Mingyang Zhang<sup>1</sup>, Joe Berry<sup>2</sup>, Yoichi Paolo Shiga<sup>3</sup>, Russell Doughty<sup>4</sup>, Nima Madani<sup>5</sup>, Xing Li<sup>6</sup>, Jingfeng Xiao<sup>7</sup>, Jiaming Wen<sup>8</sup>, Ying Sun<sup>8</sup>, Ruixue Lei<sup>1</sup>, and Scot Miller<sup>1</sup>

<sup>1</sup>Johns Hopkins University

<sup>2</sup>Carnegie Institution for Science

<sup>3</sup>Independent Researcher

<sup>4</sup>California Institute of Technology

<sup>5</sup>Jet Propulsion Laboratory

<sup>6</sup>Seoul National University

<sup>7</sup>University of New Hampshire

<sup>8</sup>Cornell University

December 7, 2022

## Abstract

Solar-induced fluorescence (SIF) shows enormous promise as a proxy for photosynthesis and as a tool for modeling variability in gross primary productivity (GPP) and net biosphere exchange (NBE). In this study, we explore the skill of SIF and other vegetation indicators in predicting variability in global atmospheric CO<sub>2</sub> observations, and thus global variability in NBE. We do so using a four-year record of global CO<sub>2</sub> observations from NASA's Orbiting Carbon Observatory 2 (OCO-2) satellite and using a geostatistical inverse model. We find that existing SIF products closely correlate with space-time variability in atmospheric CO<sub>2</sub> observations in the extra-tropics but show weaker explanatory power across the tropics. In the extra-tropics, all SIF products exhibit greater skill in explaining variability in atmospheric CO<sub>2</sub> observations compared to an ensemble of process-based CO<sub>2</sub> flux models and other vegetation indicators. Furthermore, we find that using SIF as a predictor variable in the geostatistical inverse model shifts the seasonal cycle of estimated NBE and yields an earlier end to the growing season relative to other vegetation indicators. In tropical biomes, by contrast, the seasonal cycles of SIF products and estimated NBE are out of phase, and existing respiration and biomass burning estimates do not reconcile this discrepancy. Overall, our results highlight several advantages and challenges of using SIF products to help predict global variability in GPP and NBE.

# Solar-induced fluorescence products show variable skill in constraining global patterns in biospheric CO<sub>2</sub> fluxes

Mingyang Zhang<sup>1</sup>, Joseph A. Berry<sup>2</sup>, Yoichi P. Shiga<sup>3</sup>, Russell B. Doughty<sup>4</sup>,  
Nima Madani<sup>5,6</sup>, Xing Li<sup>7</sup>, Jingfeng Xiao<sup>8</sup>, Jiaming Wen<sup>9</sup>, Ying Sun<sup>9</sup>, Ruixue  
Lei<sup>1</sup>, Scot M. Miller<sup>1</sup>

<sup>1</sup>Department of Environmental Health and Engineering, Johns Hopkins University, Baltimore, MD, USA

<sup>2</sup>Department of Global Ecology, Carnegie Institution for Science, Stanford, CA, USA

<sup>3</sup>Independent Researcher, San Francisco, CA, USA

<sup>4</sup>College of Atmospheric & Geographic Sciences, University of Oklahoma, Norman, OK, USA

<sup>5</sup>Jet Propulsion Laboratory, California Institute of Technology, Pasadena, CA

<sup>6</sup>UCLA Joint Institute for Regional Earth System Science and Engineering, Los Angeles, CA

<sup>7</sup>Research Institute of Agriculture and Life Sciences, Seoul National University, Seoul, South Korea

<sup>8</sup>Earth Systems Research Center, Institute for the Study of Earth, Oceans, and Space, University of New

Hampshire, Durham, NH, USA

<sup>9</sup>School of Integrative Plant Science, Soil and Crop Sciences Section, Cornell University, Ithaca, NY, USA

## Key Points:

- SIF products adeptly explain variability in atmospheric CO<sub>2</sub> observations, and thus in CO<sub>2</sub> fluxes, in the extra-tropics but not the tropics.
- Inverse model estimates of net biospheric exchange (NBE) that are informed by SIF exhibit a different seasonal cycle in the extra-tropics
- The seasonal cycle of SIF products in tropical biomes is out of phase with inverse estimates of NBE.

---

Corresponding author: Mingyang Zhang, [mzhang78@jhu.edu](mailto:mzhang78@jhu.edu)

## Abstract

Solar-induced fluorescence (SIF) shows enormous promise as a proxy for photosynthesis and as a tool for modeling variability in gross primary productivity (GPP) and net biosphere exchange (NBE). In this study, we explore the skill of SIF and other vegetation indicators in predicting variability in global atmospheric CO<sub>2</sub> observations, and thus global variability in NBE. We do so using a four-year record of global CO<sub>2</sub> observations from NASA’s Orbiting Carbon Observatory 2 (OCO-2) satellite and using a geostatistical inverse model. We find that existing SIF products closely correlate with space-time variability in atmospheric CO<sub>2</sub> observations in the extra-tropics but show weaker explanatory power across the tropics. In the extra-tropics, all SIF products exhibit greater skill in explaining variability in atmospheric CO<sub>2</sub> observations compared to an ensemble of process-based CO<sub>2</sub> flux models and other vegetation indicators. Furthermore, we find that using SIF as a predictor variable in the geostatistical inverse model shifts the seasonal cycle of estimated NBE and yields an earlier end to the growing season relative to other vegetation indicators. In tropical biomes, by contrast, the seasonal cycles of SIF products and estimated NBE are out of phase, and existing respiration and biomass burning estimates do not reconcile this discrepancy. Overall, our results highlight several advantages and challenges of using SIF products to help predict global variability in GPP and NBE.

## 1 Introduction

CO<sub>2</sub> uptake by photosynthesis, also known as gross primary productivity (GPP), is a key driver of the carbon cycle (e.g., Beer et al., 2010; Field et al., 1995). However, global-scale patterns in GPP are difficult to estimate. For example, terrestrial biospheric flux models (TBMs) give widely different estimates of GPP; models do not show consensus on the global magnitude of GPP, seasonal amplitude, or inter-annual variability – often due to divergent model responses to environmental conditions (e.g., Anav et al., 2015; Huntzinger et al., 2012, 2017). Huntzinger et al. (2012) further argue that uncertainties in estimated GPP dominate uncertainties in modeled net biospheric exchange (NBE), at least in an analysis of North America. In addition to models, multiple data-driven GPP estimates are available, like those generated from eddy flux towers. However, eddy flux sites are unevenly distributed across the globe, and the data are often up-scaled using machine learning algorithms to obtain a global GPP estimate (Jung et al., 2019). These estimates also show numerous differences relative to TBMs (Jung et al., 2020).

These uncertainties have motivated a longstanding interest in generating remote sensing products that can help predict space-time patterns in GPP. Numerous studies have argued that solar-induced fluorescence (SIF) holds particular promise in this regard (e.g., Damm et al., 2015; Frankenberg et al., 2011; Guan et al., 2015; Guanter et al., 2014; Köhler et al., 2018; X. Li, Xiao, & He, 2018; X. Li, Xiao, He, Arain, et al., 2018; Luus et al., 2017; MacBean et al., 2018; Shiga et al., 2018a; Y. Sun et al., 2018; Verma et al., 2017; Wood et al., 2017). SIF is radiation emitted in the red and near-infrared by chlorophyll. Hence, it can serve as an indicator of sunlight absorption by chlorophyll and therefore has the potential as a predictor of photosynthesis in plants. In the past decade, a growing number of space-based sensors provide information on SIF, opening a new window into studying photosynthesis and GPP at local to global spatial scales.

Over the past decade, there has been a profusion of research on SIF and the carbon cycle. Several studies quantify the relationships between SIF and GPP, explore the linearity or non-linearity of those relationships, and how those relationships vary across different vegetation types (e.g., A. Chen et al., 2021; Gu et al., 2019; Helm et al., 2020; Kim et al., 2021; Z. Li et al., 2020; X. Li & Xiao, 2022; Magney et al., 2017; Magney, Frankenberg, et al., 2019; Marrs et al., 2020; Y. Sun et al., 2018; Verma et al., 2017; Wood

74 et al., 2017). Additional studies explore how SIF varies during climate anomalies like heat-  
75 waves or drought (e.g., Guan et al., 2016; He et al., 2019; Helm et al., 2020; Jiao et al.,  
76 2019; Shekhar et al., 2020; L. Zhang et al., 2019).

77 In general, most studies show a close correlation between SIF and GPP at space-  
78 time scales that are observable by current satellite observations of SIF (e.g., Franken-  
79 berg et al., 2011; Guanter et al., 2012, 2014; X. Li, Xiao, He, Arain, et al., 2018; Y. Sun  
80 et al., 2018; Verma et al., 2017; Wood et al., 2017). By contrast, the relationship between  
81 SIF and GPP can be non-linear and/or weak at the scale of individual leaves or plants,  
82 partly due to variability in photosynthetic efficiency at these scales (e.g., Magney et al.,  
83 2020). With that said, the non-linearities found at sub-canopy scales often average out  
84 at kilometer spatial scales (Magney et al., 2020) and when SIF is upscaled from instan-  
85 taneous to daily or monthly scales (e.g., Hu et al., 2018; Pierrat et al., 2022). Specifi-  
86 cally, SIF-GPP relationships are likely strongest across coarser space-time scales where  
87 GPP closely correlates with absorbed photosynthetically active radiation (APAR) (e.g.,  
88 Magney et al., 2020; Marrs et al., 2020).

89 Numerous works also compare and contrast SIF against other vegetation indica-  
90 tors that are commonly used to model the global carbon cycle, including the enhanced  
91 vegetation index (EVI) and normalized difference vegetation index (NDVI) (e.g., Chang  
92 et al., 2019; Doughty et al., 2021; Jeong et al., 2017; Magney, Bowling, et al., 2019; Shiga  
93 et al., 2018a; Yang et al., 2015; J. Zhang et al., 2022; Zuromski et al., 2018). In general,  
94 SIF appears to reflect changes in GPP induced by seasonal or climate-related variabil-  
95 ity more quickly than either EVI or NDVI (e.g., Luus et al., 2017; Jeong et al., 2017; Mag-  
96 ney, Bowling, et al., 2019; Meroni et al., 2009; Shekhar et al., 2020; F. Wang et al., 2020).

97 In addition to SIF, another vegetation indicator, known as the near-infrared reflectance  
98 of vegetation (NIRv), has recently gained attention as a potential proxy for GPP. NIRv  
99 is the estimated portion of near-infrared (NIR) reflectance that is due to vegetation (Badgley  
100 et al., 2017, 2019; Dechant et al., 2020, 2022). One motive for the creation of NIRv is  
101 to decrease contamination due to non-vegetation (branches, litter, etc.) that can be present  
102 in other vegetation indicators like EVI and NDVI. Existing studies show that NIRv cor-  
103 relates with GPP (Badgley et al., 2017), largely because NIRv indicates variation in canopy  
104 structure, which was shown to correlate with light use efficiency and GPP at several crop  
105 sites (Dechant et al., 2020).

106 There has also been substantial interest in incorporating SIF within TBMs to im-  
107 prove regional to global estimates of GPP and NBE (e.g., Bacour et al., 2019; Luus et  
108 al., 2017; MacBean et al., 2018; Parazoo et al., 2020; Thum et al., 2017). However, it is  
109 challenging to evaluate the relationships between SIF and GPP or NBE across large re-  
110 gions and across the entire globe. For example, existing studies often evaluate these re-  
111 lationships at eddy flux sites, which have a very localized footprint (e.g., Dechant et al.,  
112 2022; S. Wang et al., 2021; Wood et al., 2017) or evaluate these relationships across larger  
113 regions using model estimates of GPP (e.g., Byrne et al., 2018; Frankenberg et al., 2011;  
114 Verma et al., 2017).

115 Atmospheric CO<sub>2</sub> observations, by contrast, provide an opportunity to evaluate the  
116 skill of vegetation indicators in describing space-time variability in GPP and NBE across  
117 larger regions. Satellites like OCO-2 provide global coverage of CO<sub>2</sub> observations, includ-  
118 ing regions with sparse ground-based atmospheric or eddy flux CO<sub>2</sub> data. The task of  
119 evaluating vegetation indicators using atmospheric CO<sub>2</sub> observations entails several chal-  
120 lenges. First, atmospheric observations are influenced by all types of CO<sub>2</sub> fluxes, not just  
121 GPP. Second, atmospheric CO<sub>2</sub> observations do not provide a direct measure of surface  
122 CO<sub>2</sub> fluxes and typically necessitate an atmospheric model and/or inverse model to re-  
123 late observations to surface fluxes.

Several existing studies provide a possible road map for how to connect atmospheric CO<sub>2</sub> observations with vegetation indicators. For example, a handful of studies directly compare the seasonal cycles of SIF against satellite-based CO<sub>2</sub> observations across the Amazon (e.g., Parazoo et al., 2013; Albright et al., 2022); these studies report that the seasonality of SIF and atmospheric CO<sub>2</sub> are modestly anti-correlated, implying that GPP is driving the seasonality of NBE in this region (Parazoo et al., 2013). Additional studies use SIF to help interpret space-time patterns in NBE estimated using atmospheric CO<sub>2</sub> observations and inverse modeling (e.g., Liu et al., 2017, 2020; Byrne et al., 2021).

Shiga et al. (2018a) use a different approach to evaluate vegetation indicators using atmospheric CO<sub>2</sub> observations across North America. The authors estimate NBE using a geostatistical inverse model (GIM) that is paired with an atmospheric transport model. They test out different vegetation indicators as predictor variables of NBE within the inverse model and evaluate how well each helps the inverse model match atmospheric CO<sub>2</sub> observations. Using this framework, the authors find a stronger correlation between atmospheric CO<sub>2</sub> observations and SIF relative to other vegetation indicators. The authors posit that SIF better captures peak CO<sub>2</sub> uptake in croplands and better describes seasonal transitions in boreal evergreen forests.

In the present study, we use atmospheric CO<sub>2</sub> observations and a GIM to evaluate the ability of SIF products, NIRv, and other vegetation indicators to help constrain global patterns in NBE. We are particularly interested in why SIF products are (or are not) better predictors of space-time variability in atmospheric CO<sub>2</sub> observations relative to other vegetation indicators. We then compare the ability of SIF products to help describe variability in atmospheric CO<sub>2</sub> observations against state-of-the-art TBMs. We are also interested in how estimated NBE changes globally when we use different vegetation indicators as predictors.

## 2 Methods

The overall approach in this study is to incorporate different vegetation indicators as predictor variables of NBE in a geostatistical inverse model (GIM). The GIM is fitted to global CO<sub>2</sub> observations from OCO-2 or in situ CO<sub>2</sub> observations. The approach used here follows that of Shiga et al. (2018a), who evaluate the relationships between SIF and NBE across North America using in situ CO<sub>2</sub> observations. It also builds upon the methodology developed in previous GIM studies using both in situ and satellite CO<sub>2</sub> observations (e.g., Gourdjji et al., 2008; Shiga et al., 2018b; S. M. Miller et al., 2020a; Z. Chen et al., 2021a, 2021b).

### 2.1 The atmospheric inverse model

A GIM will produce an estimate of CO<sub>2</sub> fluxes (in this case, the sum of NBE, anthropogenic emissions, and ocean fluxes) using atmospheric CO<sub>2</sub> observations, an atmospheric transport model, and predictor variables of CO<sub>2</sub> fluxes. Specifically, a GIM models CO<sub>2</sub> fluxes as the sum of two different components (e.g., Kitanidis & Vomvoris, 1983; Michalak et al., 2004; Fang et al., 2014; Z. Chen et al., 2021a):

$$\mathbf{s} = \mathbf{X}\boldsymbol{\beta} + \boldsymbol{\zeta} \quad (1)$$

The first component ( $\mathbf{X}\boldsymbol{\beta}$ ) is a linear model of different predictor variables that may help describe variability in NBE. In the above equation,  $\mathbf{s}$  are total CO<sub>2</sub> fluxes, the sum of NBE, ocean fluxes, and anthropogenic emissions. The dimensions of  $\mathbf{s}$  are  $m \times 1$ , where  $m$  is the number of model grid cells at all different times and locations. The variable  $\mathbf{X}$  is a matrix of different predictor variables, and each column of  $\mathbf{X}$  is a different predictor. If there are  $p$  predictor variables, then  $\mathbf{X}$  has dimensions  $m \times p$ . In previous studies, these predictor variables have included vegetation indicators, environmental data (e.g., estimates of soil moisture or PAR), estimates of biomass burning CO<sub>2</sub> fluxes, estimates

173 of ocean CO<sub>2</sub> fluxes, and estimates of anthropogenic CO<sub>2</sub> emissions (e.g., Gourdjji et al.,  
 174 2008, 2012; Fang et al., 2014; Fang & Michalak, 2015; Shiga et al., 2018a, 2018b; Z. Chen  
 175 et al., 2021a, 2021b). The coefficients ( $\beta$ , dimensions  $p \times 1$ ) scale the overall magnitude  
 176 of each predictor variable. These coefficients are estimated as part of the GIM to opti-  
 177 mize the model fit against CO<sub>2</sub> observations, a topic discussed later in this section.

178 It is unlikely that any combination of predictor variables will be able to perfectly  
 179 match actual CO<sub>2</sub> fluxes (e.g., Gourdjji et al., 2008, 2012; Z. Chen et al., 2021a). There  
 180 may be errors in these predictor variables, and/or there may be complex processes gov-  
 181 erning NBE that cannot be explained by a linear combination of available predictor vari-  
 182 ables. In the second component of Eq. 1, denoted  $\zeta$  (dimensions  $m \times 1$ ), the GIM will  
 183 quantify additional patterns in CO<sub>2</sub> fluxes such that the CO<sub>2</sub> flux estimate better matches  
 184 atmospheric CO<sub>2</sub> observations (e.g., Michalak et al., 2004). This component can vary  
 185 in each model grid box and at each time step (in this case, each day).

186 Note that we subtract anthropogenic emissions from our estimate of  $s$  to obtain  
 187 an estimate of NBE. In this study, we use an anthropogenic emissions estimate from the  
 188 Open-source Data Inventory for Anthropogenic CO<sub>2</sub> (ODIAC, Oda et al., 2018) as a  
 189 predictor variable in  $\mathbf{X}$ , and we subsequently subtract ODIAC from our estimate of  $s$   
 190 to obtain an estimate of NBE. Note that it is standard practice in existing inverse mod-  
 191 eling studies of CO<sub>2</sub> to subtract the influence of anthropogenic emissions in order to ob-  
 192 tain an estimate of NBE (e.g., Gourdjji et al., 2012; Z. Chen et al., 2021a, 2021b; Peiro  
 193 et al., 2022). We do not attempt to further partition the NBE estimate into GPP, res-  
 194 piration, or biomass burning fluxes. We argue that the atmospheric CO<sub>2</sub> observations  
 195 used in this study do not provide sufficient information to confidently partition the NBE  
 196 estimate into these categories. Furthermore, no existing GIM study has attempted this  
 197 type of partitioning (e.g., Michalak et al., 2004; Gourdjji et al., 2008, 2012; Fang et al.,  
 198 2014; Fang & Michalak, 2015; Shiga et al., 2018a, 2018b; Z. Chen et al., 2021a, 2021b).

199 The CO<sub>2</sub> fluxes from the inverse model ( $s$ ), when passed through an atmospheric  
 200 model ( $h()$ ), should match atmospheric CO<sub>2</sub> observations ( $z$ ) (e.g., Fang et al., 2014; Z. Chen  
 201 et al., 2021a):

$$202 \quad z = h(s) + \epsilon \quad (2)$$

203 Specifically, the CO<sub>2</sub> fluxes ( $s$ ) should match the atmospheric observations ( $z$ ) within  
 204 a margin of error specified by the inverse modeler ( $\epsilon$ ). The variance of  $\epsilon$  needs to be spec-  
 205 ified by the user before running the inverse model, and this point is discussed in greater  
 206 detail in the SI.  $z$  and  $\epsilon$  have dimensions  $n \times 1$ , where  $n$  are the number of observations.  
 207 In this study, we use 10-second averages of version 10r CO<sub>2</sub> observations from OCO-2  
 208 (land nadir, land glint, and target observations only) (e.g. Peiro et al., 2022) and in situ  
 209 observations from the NOAA CO<sub>2</sub> Obspack v3.2 developed for the OCO-2 model inter-  
 210 comparison project (MIP) (NOAA Global Monitoring Laboratory, 2021). In addition,  
 211 we use the GEOS-Chem forward and adjoint models (version 9-02) for the atmospheric  
 212 transport ( $h()$ ). The global simulations here are driven by winds from the Modern-Era  
 213 Retrospective Analysis for Research and Applications 2 (MERRA-2) (Gelaro et al., 2017)  
 214 and have a spatial resolution of 4° latitude by 5° longitude. Furthermore, the simula-  
 215 tions in this study cover September 2014 through December 2018. Note that we initial-  
 216 ize model simulations for September 2014 using estimated atmospheric CO<sub>2</sub> fields from  
 217 NOAA’s CarbonTracker CT2019 product (Jacobson et al., 2020). We discard 2014 as  
 218 a model spin-up period, following the procedure used in Z. Chen et al. (2021a) and Z. Chen  
 219 et al. (2021b).

220 Both the CO<sub>2</sub> fluxes ( $s$ ) and coefficients ( $\beta$ ) are unknown and must be estimated  
 221 as part of the GIM. The coefficients are calculated by solving a linear equation (e.g., Fang  
 222 et al., 2014; Z. Chen et al., 2021a):

$$223 \quad \hat{\beta} = (h(\mathbf{X})^T \Psi^{-1} h(\mathbf{X}))^{-1} h(\mathbf{X})^T \Psi^{-1} z \quad (3)$$

224 In this equation,  $\Psi$  (dimensions  $n \times n$ ) is a covariance matrix that describes the uncer-  
 225 tainties in the model-data system (i.e., describes the residuals  $\mathbf{z} - h(\mathbf{X}\boldsymbol{\beta})$ ). This ma-  
 226 trix is defined by the modeler and is described in more detail in the SI. Furthermore, this  
 227 equation requires inputting each vegetation indicator and predictor variable into the at-  
 228 mospheric transport model in place of a CO<sub>2</sub> flux estimate. In other words, we input each  
 229 vegetation indicator in GEOS-Chem as if it were a CO<sub>2</sub> flux to calculate  $h(\mathbf{X})$ . GEOS-  
 230 Chem will then translate patterns in surface-level variables like SIF into an atmospheric  
 231 tracer with patterns defined by SIF. Note that the units or absolute magnitude of the  
 232 vegetation indicators are not important in this framework (e.g., Shiga et al., 2018a, 2018b).  
 233 Rather, the coefficients ( $\boldsymbol{\beta}$ ) estimated using the GIM will scale the magnitude of each  
 234 vegetation indicator or predictor variable to create a model of CO<sub>2</sub> fluxes that optimally  
 235 matches atmospheric CO<sub>2</sub> observations ( $\mathbf{z}$ ).

236 Note that we run the GIM for the entire globe, but we estimate different coefficients  
 237 ( $\boldsymbol{\beta}$ ) for different biomes and for different years, the same approach used in S. M. Miller  
 238 et al. (2018), S. M. Miller and Michalak (2020b), Z. Chen et al. (2021a), and Z. Chen  
 239 et al. (2021b). These biomes are shown in Fig. S1 and are the same biomes used in the  
 240 aforementioned studies. This setup accounts for the fact that the relationships between  
 241 NBE and vegetation indicators like SIF may be different in boreal forests versus deserts  
 242 or tropical grasslands (e.g., A. Chen et al., 2021). We also analyze the results at this biome  
 243 level. The use of different coefficients in different years also means that the model is be-  
 244 ing fitted to spatial and seasonal variability within each year; spurious multi-year trends  
 245 in the predictor variables will not adversely impact the model-data fit. With that said,  
 246 we present the estimated coefficients ( $\hat{\boldsymbol{\beta}}$ ) and NBE estimate averaged across the four-  
 247 year study period (2015–2018). The SI, by contrast, presents year-to-year differences in  
 248 the estimated coefficients.

249 The choice of biomes here is specifically informed by several previous studies of OCO-  
 250 2 observations (S. M. Miller et al., 2018; S. M. Miller & Michalak, 2020b). These stud-  
 251 ies find that recent versions of the observations can be used to constrain NBE across large  
 252 biome-based regions in most seasons. If we attempt to estimate different coefficients ( $\boldsymbol{\beta}$ )  
 253 for smaller regions, we generally obtain unrealistic and unphysical estimates because OCO-  
 254 2 observations do not provide sufficient information to constrain the coefficients across  
 255 smaller regions. Hence, the biomes used here balance our desire to obtain detailed in-  
 256 formation about NBE with the limitations of currently-available CO<sub>2</sub> observations.

257 In contrast to the coefficients ( $\boldsymbol{\beta}$ ), estimating the CO<sub>2</sub> fluxes ( $\mathbf{s}$ ) is more involved.  
 258 This step requires minimizing a cost function (e.g., Kitanidis & Vomvoris, 1983; Michal-  
 259 lak et al., 2004):

$$260 \quad L = \frac{1}{2}(\mathbf{z} - h(\mathbf{s}))^T \mathbf{R}^{-1}(\mathbf{z} - h(\mathbf{s})) + \frac{1}{2}(\mathbf{s} - \mathbf{X}\boldsymbol{\beta})^T \mathbf{Q}^{-1}(\mathbf{s} - \mathbf{X}\boldsymbol{\beta}) \quad (4)$$

261 The first component of the cost function quantifies how well the estimated CO<sub>2</sub> fluxes  
 262 , when passed through GEOS-Chem, match the atmospheric observations ( $\mathbf{z} - h(\mathbf{s})$ , aka  
 263  $\boldsymbol{\epsilon}$ ). They should match within a margin specified by  $\mathbf{R}$  (dimensions  $n \times n$ ), a covariance  
 264 matrix defined by the modeler. The second term governs the properties of  $\boldsymbol{\zeta}$  or, equiv-  
 265 alently,  $\mathbf{s} - \mathbf{X}\boldsymbol{\beta}$  (Eq. 1).  $\boldsymbol{\zeta}$  should have spatial and temporal properties that match the  
 266 covariance matrix  $\mathbf{Q}$  (dimensions  $m \times m$ ), which is also defined by the modeler. These  
 267 covariance matrices are described in greater detail in the SI. We minimize the cost func-  
 268 tion with respect to  $\mathbf{s}$  using an iterative solver, described in S. M. Miller et al. (2020a),  
 269 Z. Chen et al. (2021a), and Z. Chen et al. (2021b).

## 270 2.2 Remote sensing vegetation indicators and predictor variables

271 We incorporate several vegetation indicators as predictor variables of NBE in the  
 272 GIM. We specifically use four different SIF products based on SIF retrievals from OCO-  
 273 2 – SIF<sub>OCO2\_005</sub> (Yu et al., 2019a), CSIF (Y. Zhang et al., 2018), GOSIF (X. Li & Xiao,

274 2019b), and a SIF product from scientists at the Jet Propulsion Laboratory (referred to  
 275 as JPL SIF) (Madani et al., 2022). The first three products are created by interpolat-  
 276 ing SIF retrievals from OCO-2 onto a global grid using machine learning algorithms. The  
 277 last product (JPL SIF) is created by binning high-quality OCO-2 SIF retrievals into monthly,  
 278  $4^\circ$  latitude by  $4^\circ$  longitude grid boxes and taking a simple mean of all retrievals in each  
 279 grid box. Note that other satellite sensors also provide SIF retrievals (e.g., the Green-  
 280 house Gases Observing Satellite (GOSAT) and the TROPospheric Monitoring Instru-  
 281 ment (TROPOMI)), but we specifically use SIF products from OCO-2 retrievals because  
 282 these products are available for the same time period as the modeling simulations in this  
 283 study (2015–2018) and are generated from the same satellite (OCO-2) as the  $\text{CO}_2$  ob-  
 284 servations used in this study.

285 Although all four SIF products are based on OCO-2 SIF observations, these prod-  
 286 ucts show several notable differences. First, the JPL SIF product is based on a much sim-  
 287 pler method than any of the machine-learning (ML) based products. Second, different  
 288 OCO-2 SIF retrievals are used in these products. GOSIF and CSIF use the 757 nm wave-  
 289 length, while  $\text{SIF}_{\text{OCO2}.005}$  uses the average of 757nm and 771 nm wavelengths, and JPL  
 290 SIF uses the 740 nm wavelength. Third, although three of the four SIF products are ML-  
 291 based, they use either a Cubist regression tree-based method (GOSIF) or feed-forward  
 292 neural networks (CSIF and  $\text{SIF}_{\text{OCO2}.005}$ ). However, Wen et al. (2020) find a similar pre-  
 293 diction performance of these two types of ML methods, and therefore the difference in  
 294 the ML method alone may not yield notable differences in the final SIF products. Fourth,  
 295 different sets of predictor variables are used in each of the three ML-based products. The  
 296 nadir bidirectional reflectance distribution adjusted reflectance (NBAR) from MODIS  
 297 is the only predictor in the model for CSIF (MCD43C4) and  $\text{SIF}_{\text{OCO2}.005}$  (MCD43A4  
 298 and MCD43C4) products, and the MCD43 surface reflectance may contain some miss-  
 299 ing values in tropical forests due to clouds (Yu et al., 2019a; Y. Zhang et al., 2018). By  
 300 contrast, the GOSIF study does not include the MODIS NBAR as a predictor. Instead,  
 301 they use environmental data such as EVI from MODIS (MCD12), PAR, vapor pressure  
 302 deficit, and air temperature from MERRA-2 (X. Li & Xiao, 2019b). Lastly, these stud-  
 303 ies use different strategies to fit the ML model. Specifically, GOSIF and CSIF are fit-  
 304 ted globally, while  $\text{SIF}_{\text{OCO2}.005}$  is fitted separately for each individual biome.

305 Note that for the setup here, we aggregate the GOSIF, CSIF, and  $\text{SIF}_{\text{OCO2}.005}$  prod-  
 306 ucts and other predictor variables (described below) to a 16-day time resolution before  
 307 inputting them into the GIM, ensuring a fairer comparison among different GIM sim-  
 308 ulations using different vegetation indicators (e.g., Shiga et al., 2018a; Z. Chen et al., 2021a).  
 309 Note that JPL SIF is available at a monthly time resolution; OCO-2 SIF observations  
 310 are spatially sparse, and the monthly time resolution ensures that there are enough ob-  
 311 servations in each grid box to obtain a reliable mean. Refer to SI Sect. S3 for more dis-  
 312 cussion of this point.

313 In addition to SIF, we also include several additional vegetation indicators as pre-  
 314 dictor variables in the inverse model – NDVI, EVI, and  $\text{NIR}_v$ . NDVI is the difference  
 315 between NIR reflectance and visible red reflectance, divided by the sum of these two quan-  
 316 tities (e.g., NASA, 2000). Green vegetation reflects in the NIR but not in the visible red,  
 317 and NDVI therefore provides a measure of vegetation greenness. EVI additionally in-  
 318 cludes a correction for atmospheric effects and background noise (e.g., USGS, 2022). We  
 319 use 16-day EVI and NDVI from MODIS Terra (product MOD13C1 with best, good, and  
 320 mixed quality assurance flags; QA = 0, 1 and 2, respectively).  $\text{NIR}_v$ , by contrast, is the  
 321 product of vegetation indicator NIR reflectance and NDVI, and we construct  $\text{NIR}_v$  us-  
 322 ing red (620–670 nm) and NIR (841–876 nm) reflectance data from MODIS Terra (prod-  
 323 uct MCD43, reflectance bands 1 and 2). We further re-grid each product from the origi-  
 324 nal  $0.05^\circ$  by  $0.05^\circ$  degree resolution provided by NASA to the  $4^\circ$  by  $5^\circ$  resolution of GEOS-  
 325 Chem.

326 In addition to these vegetation indicators, we include environmental driver data  
 327 (e.g., estimated meteorological variables) as predictor variables of NBE. These additional  
 328 predictor variables may help account for space-time variability in respiration, and may  
 329 describe additional patterns in GPP not described by the vegetation indicators. The use  
 330 of environmental driver data in the GIM follows numerous existing studies (Gourdji et  
 331 al., 2008, 2012; Fang et al., 2014; Fang & Michalak, 2015; Shiga et al., 2018a, 2018b; Z. Chen  
 332 et al., 2021a, 2021b). We specifically consider driver data from MERRA-2 – 2 m air tem-  
 333 perature, precipitation, PAR, surface downwelling shortwave radiation, soil temperature  
 334 at 10 cm depth, soil moisture at 10 cm depth, specific humidity, and relative humidity.  
 335 We also include a non-linear function of air temperature from Mahadevan et al. (2008).  
 336 In a recent GIM study using CO<sub>2</sub> observations from OCO-2, Z. Chen et al. (2021a) find  
 337 that air temperature is a poor predictor variable and does little to help the inverse model  
 338 describe patterns in CO<sub>2</sub> observations. Rather, they find that a non-linear function of  
 339 air temperature has much better explanatory power in the GIM. Refer to SI Sect. S3  
 340 for a discussion of uncertainties in these environmental driver data.

341 We do not assimilate all of these environmental driver data from MERRA-2 as pre-  
 342 dictor variables in the GIM; several of these variables are highly correlated or colinear  
 343 and including all of these variables would likely overfit the CO<sub>2</sub> observations from OCO-  
 344 2 and in situ sites. Instead, we use model selection based on the Bayesian Information  
 345 Criterion (BIC) to determine which combination of variables in different biomes can best  
 346 complement the vegetation indicators and optimize model-data fit against CO<sub>2</sub> obser-  
 347 vations from OCO-2. Numerous GIM studies to date employ the BIC to decide on a set  
 348 of environmental predictor variables for the GIM (e.g., Gourdji et al., 2012; Fang et al.,  
 349 2014; Fang & Michalak, 2015; S. Miller et al., 2014a; S. M. Miller et al., 2016a; Shiga  
 350 et al., 2018a, 2018b; Z. Chen et al., 2021a, 2021b). Furthermore, the approach used here  
 351 mirrors that used in Z. Chen et al. (2021a) and Z. Chen et al. (2021b) and is described  
 352 in greater detail in the Supplement.

353 In some GIM simulations (e.g., Sect. 3.3), we also consider respiration estimates  
 354 from an ensemble of TBMs for use as predictor variables in the GIM. We specifically in-  
 355 corporate respiration estimates from 15 flux models that are part of the Global Carbon  
 356 Projects’ Trends in Net Land Atmosphere Carbon Exchanges (TRENDY) model inter-  
 357 comparison (version 8, Friedlingstein et al., 2019; Sitch et al., 2015). Note that we use  
 358 TRENDY scenario three, which includes all forcings (e.g., climate and land use forcings).  
 359 These respiration estimates are available for the time period of this study (2014–2018)  
 360 and are reported at variable spatial resolution and monthly temporal resolution, described  
 361 in the Supplement.

362 All model simulations in this study further include estimates for other CO<sub>2</sub> source  
 363 types: fossil fuel fluxes from ODIAC (Oda et al., 2018), ocean fluxes from the Circula-  
 364 tion and Climate of the Ocean consortium (ECCO-Darwin, Carroll et al., 2020), and  
 365 Global Fire Emissions Database (GFED) version 4.1 (Giglio et al., 2013). These flux es-  
 366 timates are incorporated as predictor variables in the GIM (in  $\mathbf{X}$ , as in Z. Chen et al.,  
 367 2021a, 2021b).

### 368 **2.3 Analysis using the inverse model and predictor variables**

369 We use the inverse model or GIM to conduct two analyses. In the first analysis,  
 370 we evaluate how well we are able to reproduce patterns in atmospheric CO<sub>2</sub> observations  
 371 using a linear model of vegetation indicators and other predictor variables. For this anal-  
 372 ysis, we use the first component of the CO<sub>2</sub> flux estimate from the GIM ( $\mathbf{X}\boldsymbol{\beta}$  in Eq. 1).  
 373 We input this component of the flux estimate into GEOS-Chem and compare the results  
 374 against CO<sub>2</sub> observations. This linear model provides a convenient way to evaluate veg-  
 375 etation indicators like SIF and NIRv using atmospheric CO<sub>2</sub> observations.

376 For the second analysis, we investigate how NBE estimated by the inverse model  
 377 changes when we incorporate different vegetation indicators as predictors. For this anal-  
 378 ysis, we evaluate the full NBE estimate from different GIM simulations that use differ-  
 379 ent vegetation indicators. This analysis illustrates the potential of SIF products to in-  
 380 form inverse estimates of NBE; it highlights the additional information on NBE provided  
 381 by SIF products compared to inverse estimates of NBE using other vegetation indica-  
 382 tors (e.g., Shiga et al., 2018a). Note that estimating the linear model ( $\mathbf{X}\boldsymbol{\beta}$ ) using Eq.  
 383 3 requires relatively little computing time while estimating NBE using Eq. 4 requires  
 384 several weeks on a supercomputer cluster. Hence, we only discuss a few representative  
 385 examples for this second set of analyses using estimated NBE.

386 The vegetation indicators evaluated here are often used as proxies for GPP, and  
 387 we acknowledge that GPP is not the only component of NBE. With that said, we ar-  
 388 gue that atmospheric CO<sub>2</sub> observations and the GIM can help inform the use of these  
 389 vegetation indicators. First, in many biomes, GPP likely dominates large-scale space-  
 390 time patterns in NBE (e.g., Parazoo et al., 2013; Shiga et al., 2018a; W. Sun et al., 2021).  
 391 Specifically, GPP is a large component of NBE, and other flux processes like autotrophic  
 392 respiration likely exhibit similar seasonal patterns as GPP (albeit with opposite sign)  
 393 (e.g., Huntzinger et al., 2012). Furthermore, existing regional-scale atmospheric stud-  
 394 ies show a correlation between GPP and NBE in both tropical and extra-tropical regions  
 395 (e.g., Parazoo et al., 2013; Shiga et al., 2018a; W. Sun et al., 2021).

396 Second, our primary goal is not to evaluate the absolute performance of the GIM  
 397 relative to atmospheric CO<sub>2</sub> observations. Rather, we are interested in the relative per-  
 398 formance of simulations that use vegetation indicators as one of several predictor vari-  
 399 ables of NBE. Uncertainties in GFED and the environmental driver data, among other  
 400 uncertainties, could lower overall model performance relative to the CO<sub>2</sub> observations,  
 401 but these uncertainties are unlikely to erroneously make one vegetation indicator appear  
 402 more skilled than another.

403 Third, in instances where SIF products do not show favorable results in the GIM  
 404 compared to other vegetation indicators, we also examine the possible role of uncertain-  
 405 ties in respiration and biomass burning to explain the discrepancies.

### 406 3 Results and discussion

#### 407 3.1 Summary of global results

408 A linear model of SIF products is able to describe substantial variability in CO<sub>2</sub>  
 409 observations from OCO-2. Specifically, a model that consists of a linear combination of  
 410 SIF products can describe between 40–85% of all variability in the OCO-2 observations,  
 411 depending upon the biome (Fig. 1a). This result reaffirms the skill of SIF to describe  
 412 regional spatial and seasonal patterns in NBE. Existing studies using atmospheric CO<sub>2</sub>  
 413 observations indicate a strong correlation between SIF and NBE in a handful of regions  
 414 – across southern Amazonia (Parazoo et al., 2013) and across North America (Shiga et  
 415 al., 2018a), and this study suggests strong correlations across much broader global biomes.

416 SIF products are also more skilled at predicting variability in CO<sub>2</sub> observations com-  
 417 pared to other vegetation indicators, at least in the extra-tropics (Fig. 1a). In these biomes,  
 418 model-data comparisons using the SIF-based linear model show higher R<sup>2</sup> values com-  
 419 pared to models based on EVI, NDVI, and NIRv (Fig. 1a). Indeed, this result comple-  
 420 ments several studies of eddy flux data that show a stronger relationship between SIF  
 421 and GPP than NDVI or EVI and GPP (e.g., Guan et al., 2016; Magney, Bowling, et al.,  
 422 2019; Shiga et al., 2018a; Yang et al., 2015; J. Zhang et al., 2022; Zuromski et al., 2018).  
 423 It also mirrors regional studies that find large-scale, seasonal decoupling between GPP  
 424 and measures of greenness like EVI and NDVI in numerous extra-tropical biomes (e.g.,  
 425 Walther et al., 2016; Jeong et al., 2017; Luus et al., 2017; Pierrat et al., 2021). In Sect.

426 3.2, we discuss in detail why a linear model of SIF is a better fit against OCO-2 obser-  
427 vations in the extra-tropics, and we explore how inverse estimates of NBE that are in-  
428 formed by SIF differ from those informed by other vegetation indicators.

429 By contrast, SIF products do not show the same advantage relative to other veg-  
430 etation indicators in the tropics (Fig. 1a). Linear models using SIF products, EVI, and  
431 NIRv exhibit similar  $R^2$  values relative to OCO-2 observations in tropical biomes. This  
432 topic is the focus of Sect. 3.3.

433 We also note that all model simulations (i.e., using EVI, NDVI, SIF, and NIRv)  
434 exhibit a lower  $R^2$  value relative to OCO-2 observations in the tropics (Fig. 1a). This  
435 lower model skill could be explained by the fact that NBE often has a larger seasonal  
436 cycle in the extra-tropics than in the tropics, and seasonal patterns in  $\text{CO}_2$  observations  
437 are therefore likely easier to fit in the former biomes than in the latter. In addition, the  
438 atmospheric transport model (GEOS-Chem coupled with winds from MERRA-2) may  
439 be subject to larger errors in the tropics than in the extra-tropics; OCO-2 has a sun-synchronous  
440 orbit and passes over every location at approximately 1pm local time. At this time of  
441 day, there is often heterogeneous convection in biomes like tropical forests, and these fea-  
442 tures may be challenging to model using a global chemical transport model like GEOS-  
443 Chem (e.g., Jiang et al., 2013). Relatedly, biomass burning events can also create con-  
444 vection that is difficult to capture in atmospheric transport models (e.g., S. M. Miller  
445 et al., 2008), particularly in the tropics where biomass burning emissions are highly vari-  
446 able (e.g., Giglio et al., 2013). These factors may help explain why the overall model skill  
447 is lower in the tropics than in the extra-tropics. However, it does not explain why the  
448 model simulations using SIF products do not outperform the other vegetation indica-  
449 tors like EVI or NDVI in tropical biomes, as is the case in extra-tropical biomes.

450 We further find that linear model simulations using different SIF products yield  
451 different model-data fit against  $\text{CO}_2$  observations (Fig. 1a). Globally, we find that a lin-  
452 ear model using either GOSIF or JPL SIF yields a slightly higher  $R^2$  in Fig. 1 relative  
453 to other SIF products. This result is perhaps surprising because JPL SIF is a much sim-  
454 pler product than the other SIF products (see Sect. 2.2). With that said, JPL SIF only  
455 relies on OCO-2 SIF data, while SIF products that yield lower  $R^2$  values rely on MODIS  
456 reflectance to interpolate the OCO-2 SIF data. The use of MODIS data makes it pos-  
457 sible to produce SIF estimates at a much finer spatial and temporal grid than available  
458 from JPL SIF (see Table S2), but these products may partly mirror patterns in that MODIS  
459 data instead of SIF. We focus on GOSIF in subsequent analyses – because it is one of  
460 two SIF products that yield the highest  $R^2$  values.

461 In a subsequent analysis, we add additional predictor variables to the linear model  
462 – environmental data, including precipitation and a function of air temperature (Fig. 1b;  
463 see also Sect. 2.2 and Table S4). Vegetation indicators like SIF and EVI are often used  
464 as predictors of GPP. However, atmospheric  $\text{CO}_2$  observations, like those used in the model-  
465 data comparisons here, are influenced by many different types of  $\text{CO}_2$  fluxes, including  
466 GPP and respiration. The inclusions of environmental data may help the model better  
467 describe variability in  $\text{CO}_2$  observations caused by respiration and may help describe ad-  
468 ditional variability in GPP that is not described by the vegetation indicators.

469 We find that the inclusion of additional predictor variables does little to improve  
470 the model-data fit ( $R^2$ , Fig. 1b). The result may appear surprising, yet it parallels ex-  
471 isting studies of in situ atmospheric  $\text{CO}_2$  observations focused on North America (Shiga  
472 et al., 2018a; W. Sun et al., 2021). Shiga et al. (2018a) construct a similar linear model  
473 of SIF and other vegetation indicators. They find that the inclusion of additional pre-  
474 dictor variables yields a better model-data fit in croplands but does little to change model-  
475 data fit in other North American biomes. W. Sun et al. (2021) also find that a SIF-based  
476 model is as adept at describing variability in atmospheric  $\text{CO}_2$  observations as NBE es-  
477 timates from many of the TRENDY models and from FLUXCOM. In addition, GPP es-

478 timates from TRANSCOM, TRENDY, and MsTMIP are often able to match patterns  
479 in atmospheric CO<sub>2</sub> observations as well as NBE estimates from these products.

480 Several factors may help explain why the inclusion of additional predictor variables  
481 does little to improve model-data fit. First, Shiga et al. (2018a) note that GPP and NBE  
482 are highly correlated in many regions, and this fact may explain why predictors of GPP  
483 like SIF are able to explain a large percentage of variability in atmospheric CO<sub>2</sub> obser-  
484 vations. Second, this result may also reflect the limits of using OCO-2 observations to  
485 constrain NBE. CO<sub>2</sub> observations from OCO-2 are spatially sparse and represent columns  
486 averages, and these observations are not as sensitive as many eddy flux or ground-based  
487 observations to fine-scale variability in NBE or the individual components of NBE. Hence,  
488 this result speaks to the positive ability of SIF to help predict global-scale patterns in  
489 NBE, but this result likely also speaks to the limitations of using OCO-2 observations  
490 to constrain detailed space-time patterns in NBE.

491 In the above analyses, we fit the linear model of predictor variables to CO<sub>2</sub> obser-  
492 vations from OCO-2. We also conduct a parallel analysis using CO<sub>2</sub> observations from  
493 in situ monitoring sites and find similar results (Fig. 2). This similarity indicates that  
494 the results are robust to the specific type of the CO<sub>2</sub> observations used in the analysis,  
495 and that the results in Fig. 1 are unlikely to be aliased or unduly contaminated by ob-  
496 servational errors. Note that much of the analysis in the remainder of the manuscript  
497 focuses on results using CO<sub>2</sub> observations from OCO-2 because it provides better data  
498 coverage (Fig. S2) across the tropics relative to the in situ observing network (Fig. S3).

499 We also explore year-to-year differences in model-data fit relative to atmospheric  
500 CO<sub>2</sub> observations. The first half of the study period (2015-2016) corresponds to a large  
501 El Niño event, whereas the second half of the study period (2017-2018) does not. We find  
502 that model-data fit is similar in El Niño versus non El Niño years – within an  $R^2$  of 0.05  
503 for all of the simulations using different vegetation indicators. In other words, no veg-  
504 etation indicator shows a discernible advantage in describing CO<sub>2</sub> observations during  
505 El Niño conditions.

506 We further find that the linear model using SIF products is a better model-data  
507 fit against OCO-2 observations in the extra-tropics than NBE estimates from the TBMs  
508 in TRENDY, which do not incorporate SIF (Fig. 3). We specifically compare the cor-  
509 relation ( $R^2$ ) with OCO-2 observations when we use NBE estimates from 15 different  
510 TRENDY models in place of the SIF-based linear model. Note that the vegetation in-  
511 dicators used here have a 16-day temporal resolution while the NBE estimates from TRENDY  
512 are available at a monthly resolution, though this fact is unlikely to place the TBMs a  
513 noticeable disadvantage (refer to the sensitivity study in SI Sect. S3). Furthermore, the  
514 TRENDY models have not been calibrated to CO<sub>2</sub> observations from OCO-2. These facts  
515 not withstanding, the results suggest that SIF could be beneficial for improving TBM  
516 flux estimates, at least in the extra-tropics, while the SIF products discussed here are  
517 unlikely to yield a similar benefit in the tropics.

518 Note that the inverse modeling analysis described in this section involves several  
519 uncertainties that may impact our ability to model variability in atmospheric CO<sub>2</sub> ob-  
520 servations. These include uncertain biomass burning and anthropogenic CO<sub>2</sub> emissions,  
521 NBE variability due to land use change, possible atmospheric transport errors, and is-  
522 sues related to the atmospheric CO<sub>2</sub> observations (e.g., observational errors or variabil-  
523 ity in data coverage). Indeed, these challenges are common to inverse modeling studies  
524 using atmospheric CO<sub>2</sub> observations. We specifically incorporate biomass burning emis-  
525 sions from GFED and anthropogenic emissions from ODIAC as predictor variables in  
526 the inverse model, and these sources are accounted for in all modeling simulations con-  
527 ducted in this study (Sect. 2.2). However, errors in either emissions estimate could lower  
528 the overall model-data fit relative to atmospheric CO<sub>2</sub> observations. With that said, we  
529 are primarily interested in the relative model-data fit, not absolute model-data fit, of model

530 simulations informed by SIF relative to those informed by other vegetation products. In  
531 addition, variability in NBE due to land use change may also be a source of uncertainty.  
532 Land use changes that alter GPP should also impact SIF (e.g., del Rosario Uribe & Dukes,  
533 2021; Ding et al., 2021) and should therefore be accounted for in model simulations. With  
534 that said, existing studies show that CO<sub>2</sub> observations from OCO-2 can only be used to  
535 constrain very broad, seasonal, biome-level variability in NBE (e.g., S. M. Miller et al.,  
536 2018; S. M. Miller & Michalak, 2020b). Land use changes that unfold over decades will  
537 undoubtedly change biome-level patterns in NBE but may not be detectable across the  
538 relatively short, four-year duration of this study. Lastly, atmospheric transport errors  
539 and issues related to the CO<sub>2</sub> observations undoubtedly lead to uncertainties in the in-  
540 verse model. These issues are common to inverse modeling studies and reiterate the im-  
541 portance of setting accurate uncertainties (i.e., covariance matrix parameters) within the  
542 inverse model. We discuss the covariance matrix parameters in Sect. S1.

### 543 3.2 The extra-tropics

544 In this section, we estimate NBE using SIF products and other vegetation indica-  
545 tors as predictor variables in the inverse model. We then evaluate how the resulting NBE  
546 estimates differ among these different inverse modeling simulations.

547 We find that incorporating SIF as a predictor variable in the inverse model leads  
548 to a different seasonal variability in NBE across the extra-tropics relative to an inverse  
549 model that incorporates EVI (Fig. 4). Specifically, NBE estimated using GOSIF show  
550 less CO<sub>2</sub> uptake in the fall than NBE estimated using EVI. Furthermore, we see this re-  
551 sult in all extra-tropical biomes.

552 This result, using a global-scale inverse model, parallels studies that compare veg-  
553 etation indicators against satellite-based GPP products and eddy flux observations. Sev-  
554 eral satellite-based studies report that the seasonality of greenness is decoupled from the  
555 seasonality of GPP in multiple extra-tropical biomes, including both evergreen and de-  
556 ciduous forests (e.g., Walther et al., 2016; Jeong et al., 2017; Luus et al., 2017; Y. Zhang  
557 et al., 2020). For example, Jeong et al. (2017) compare the seasonal cycle of SIF, NDVI,  
558 and satellite-based estimates of GPP for extratropical forests between 40° – 55°N lat-  
559 itude globally. They find that the growing season determined by NDVI is 46±11 days  
560 longer than estimated using SIF. Studies that leverage eddy flux observations reach sim-  
561 ilar conclusions (e.g., Churkina et al., 2005; Gonsamo et al., 2012).

562 This seasonal discrepancy is likely because leaves reduce their photosynthetic out-  
563 put during late summer and early autumn. However, their optical properties do not change  
564 as quickly, and are unlikely to be detected by greenness indicators like EVI or NDVI (e.g.,  
565 Jeong et al., 2017). This change is probably caused by a seasonal reduction in incom-  
566 ing solar radiation (e.g., Bauerle et al., 2012). Jeong et al. (2017) specifically find that  
567 seasonal changes and SIF and GPP products during fall correlate with changes in incom-  
568 ing shortwave radiation, whereas seasonal changes in greenness indicators like NDVI cor-  
569 relate with changes in temperature (e.g., F. Wang et al., 2020). Furthermore, Jeong et  
570 al. (2017) find that temperature and NDVI changes in fall are not linked to GPP and  
571 more likely reflect the timing of chlorophyll reduction and leaf drop (Jeong & Medvigy,  
572 2014). Hence, greenness indicators are less effective than SIF at predicting end-of-season  
573 changes in GPP. In addition, this decrease in photosynthetic activity could reflect drought  
574 stress as soil moisture is depleted through the summer (e.g., P. A. Schwarz et al., 2004).  
575 These seasonal changes may not be reflected in greenness indicators (e.g., Goerner et al.,  
576 2009). Also, data contamination cannot be ruled out; leaf litter and plant material that  
577 has not yet fallen from the plant can increase greenness indicators in the fall, yielding  
578 erroneous estimates for the end of growing season (e.g., Gonsamo et al., 2012; Walther  
579 et al., 2016).

580 Despite the differences between SIF and other vegetation indicators, Dechant et  
 581 al. (2022) propose multiplying greenness indicators by PAR, and they argue that the re-  
 582 sult may serve as an effective structural proxy for SIF and for photosynthesis. The au-  
 583 thors of that study focus on the product of NIRv and PAR (NIRvP) but show that other  
 584 greenness indicators, when multiplied by PAR, also correlate with SIF at multiple scales  
 585 – when compared to both tower and satellite observations. The product of greenness in-  
 586 dicators and PAR may help overcome the seasonal decoupling between greenness and  
 587 SIF, as discussed in the previous paragraph. Furthermore, the development of a SIF proxy  
 588 could hold practical applications. Such a proxy could be used in place of SIF in time pe-  
 589 riods or locations when SIF is not available. For example, satellites like OCO-2 provide  
 590 spatially sparse SIF observations, and existing studies assimilate SIF with other vege-  
 591 tation indicators in a machine learning algorithm to create interpolated SIF maps. Other  
 592 products, like those proposed by Dechant et al. (2022), may serve as a better proxy.

Dechant et al. (2022) also provide a theoretical underpinning for the multiplica-  
 tion of greenness indicators and PAR. They start with equations for GPP and SIF:

$$GPP = APAR \times LUE \quad (5)$$

$$SIF = APAR \times f_{esc} \times \Phi_F \quad (6)$$

where  $LUE$  is light use efficiency,  $f_{esc}$  is the canopy escape fraction, and  $\Phi_F$  is the flu-  
 orescence emission yield. Dechant et al. (2020) argue that  $f_{esc}$  is correlated with LUE  
 at seasonal time scales, at least at the agricultural sites examined, and that  $f_{esc}$  there-  
 fore plays a key role in the seasonal relationship between SIF and GPP. By contrast, they  
 argue that  $\Phi_F$  shows poor correlation with LUE.  $f_{esc}$  can be approximated by a green-  
 ness or vegetation indicator (VI) and fPAR (Zeng et al., 2019):

$$f_{esc} \approx VI/fPAR \quad (7)$$

where fPAR is the fraction of absorbed PAR. Given that  $APAR = PAR \times fPAR$  the  
 following relationship should hold:

$$APAR \times f_{esc} \approx VI \times PAR \quad (8)$$

593 Following this logic a greenness indicator like NIRv, EVI, and/or NDIV, when multiplied  
 594 by PAR, may be a reasonable structural proxy for SIF.

595 Indeed, we find that a linear model of NIRv  $\times$  PAR (NIRvP), EVIP, and NDVIP  
 596 are just as skilled at matching variability in CO<sub>2</sub> observations compared to a linear model  
 597 using GOSIF (Figs. 5a-b and S6). In addition, NBE estimated using EVIP exhibits a  
 598 similar seasonality in the fall relative to results using GOSIF (Fig. 5c). For the large biome-  
 599 based regions examined here, the product of greenness indicators and PAR may, in fact,  
 600 be an effective structural proxy for SIF and overcome the seasonal decoupling described  
 601 earlier in this section. By contrast to the extra-tropics, we find that multiplying vege-  
 602 tation indicators by PAR does relatively little to improve model data fit against OCO-  
 603 2 observations in the tropics (Figs. 5a-b and S6). Furthermore, these predictors actu-  
 604 ally worsens model-data fit relative to OCO-2 observations in tropical grasslands (Figs.  
 605 5a-b and S6). High levels of PAR can indicate decreased photosynthesis associated with  
 606 seasonal drought and low levels of PAR can indicate increased photosynthesis associated  
 607 with seasonal rainfall, a possible reason why PAR worsens model-data fit in tropical grass-  
 608 lands (e.g., Ma et al., 2014). The next section describes inverse modeling results for trop-  
 609 ical biomes in depth.

### 610 3.3 The tropics

611 We find that the seasonal cycle of SIF products in tropical biomes is shifted com-  
 612 pared to that of NBE estimated by the inverse model. Furthermore, we are unable to  
 613 reconcile these different seasonal cycles using existing estimates of respiration and biomass

614 burning. This seasonal mismatch may help explain why a linear model of SIF products  
 615 is not able to explain any more variability in OCO-2 observations relative to other veg-  
 616 etation indicators, a result discussed previously in Sect. 3.1.

617 This mismatch is apparent in Fig. 6, which compares the seasonal cycle of GOSIF  
 618 against two NBE estimates in different tropical biomes. In the Southern Hemisphere and  
 619 in Northern Hemisphere tropical forests, GOSIF indicates an onset of seasonal CO<sub>2</sub> up-  
 620 take before the two NBE estimates. By contrast, GOSIF predicts peak CO<sub>2</sub> uptake in  
 621 roughly the same months as the two NBE estimates. Note that the seasonal cycle of each  
 622 estimate in these panels has been normalized to have a mean of zero and a standard de-  
 623 viation of one in order to make GOSIF directly comparable with the NBE estimates. The  
 624 blue line in Fig. 6 displays NBE estimated by the inverse model. This inverse model in-  
 625 corporates GOSIF as a predictor variable, yet the the seasonal cycle of NBE looks very  
 626 different from that of GOSIF. In addition, the red line shows the NBE estimate from OR-  
 627 CHIDEE; of all TBMs in TRENDY, ORCHIDEE exhibits the best model-data fit ( $R^2$ )  
 628 compared to OCO-2 observations in the tropics (see Fig. S9). It is possible, although  
 629 unlikely, that CO<sub>2</sub> observations from OCO-2 do not provide a unique constraint on the  
 630 seasonal cycle of NBE in tropical biomes. However, the consistency between the seasonal  
 631 cycle of the inverse model and of ORCHIDEE suggest otherwise.

632 We further analyze the seasonal cycle of SIF data from the TROPOMI instrument  
 633 to see whether the seasonal cycle of SIF from this instrument is in any better agreement  
 634 with NBE estimates (Fig. 6). Note that the TROPOMI-SIF data do not cover the full  
 635 range of our study time period (Jan. 2015 to Dec. 2018), and we use a multi-year monthly  
 636 average (May 2018 to Dec. 2021) in this analysis for each tropical biome. We find that  
 637 the GOSIF and TROPOMI-SIF have similar seasonal cycles in tropical grasslands and  
 638 forests, which indicates that possible biases in the seasonal cycle of OCO-2 SIF prod-  
 639 ucts are unlikely to be the cause of the seasonal discrepancies in Fig. 6.

640 We also find that seasonal patterns in respiration and biomass burning cannot rec-  
 641 oncile the seasonal differences between SIF products and NBE. We include GOSIF and  
 642 environmental driver variables in the inverse model to help predict NBE (as in Shiga et  
 643 al., 2018a, ; Table S4). It is possible that this combination of predictors is skilled at cap-  
 644 turing space-time patterns in NBE due to GPP but not due to respiration. To explore  
 645 this possibility, we re-run the linear model 15 times and each time use a different res-  
 646 piration estimate from TRENDY in place of using environmental driver variables (Fig.  
 647 S10a). We find that these respiration estimates do little to improve the model-data fit  
 648 for the SIF-based linear model; the ORCHIDEE model reproduces variability in OCO-  
 649 2 observations better than any of the linear models using GOSIF and TRENDY respi-  
 650 ration estimates (i.e., has a higher  $R^2$ ), at least in tropical biomes (Fig. S10b).

651 Similarly, biomass burning cannot reconcile the differing seasonal cycles between  
 652 SIF products and the NBE estimates. Fig. 6 displays the seasonal cycle of biomass burn-  
 653 ing emissions from GFED. In this figure, we normalize GFED such that the seasonal cy-  
 654 cle is easier to compare against GOSIF and the NBE estimates. In most biomes, the peak  
 655 in biomass burning has similar timing to the minimum CO<sub>2</sub> uptake predicted by GOSIF.  
 656 However, this peak is earlier in most tropical biomes than the peak in NBE (i.e., max-  
 657 imum seasonal CO<sub>2</sub> release). Note that all modeling simulations in this study include  
 658 GFED as a predictor variable.

659 It is unclear why SIF products are not more skilled predictors of NBE in the trop-  
 660 ics relative to other vegetation indicators; there are several possible reasons. First, TBMs  
 661 disagree on the seasonality of respiration in the tropics, and it is possible that none of  
 662 the TBMs used here provides a skilled respiration estimate. Indeed, the seasonal mis-  
 663 match between SIF products and NBE in Fig. 6 is most pronounced around the peak  
 664 in NBE (i.e., maximum CO<sub>2</sub> release), indicating that deficiencies in the respiration es-  
 665 timates may be at play.

666 Second, the SIF products used in this study may not be an accurate representa-  
667 tion of SIF. SIF retrievals from OCO-2 must be interpolated to fill data gaps and cre-  
668 ate a continuous, gridded SIF map, and uncertainties in the gap-filling process can im-  
669 pact the accuracy of the resulting SIF products, particularly in the tropics. For exam-  
670 ple, Yu et al. (2019b) point out that SIF retrievals for some tropical regions (e.g., grass-  
671 lands and shrublands) exhibit a lower signal-to-noise ratio due to lower overall SIF val-  
672 ues in those biomes, and they explain that those biomes could experience rapid changes  
673 in photosynthesis that may not be captured by OCO-2 with a 16-day revisit time. Sub-  
674 stantial differences among the OCO-2 based SIF products further highlights the uncer-  
675 tainty associated with interpolation and gap-filling. In addition, SIF observations from  
676 OCO-2 are sensitive to atmospheric cloud/aerosol contamination or sun-sensor geom-  
677 etry which can confound the real seasonality photosynthesis, particularly in tropical forests  
678 (e.g., X. Li, Xiao, He, Arain, et al., 2018; Yu et al., 2019b).

679 Third, canopy-level and/or remotely sensed SIF may not be a skilled proxy for GPP.  
680 This explanation, however, seems less likely given that several site-level studies find good  
681 correlation between SIF and GPP in a variety of tropical biomes (e.g., C. Wang et al.,  
682 2019; Mengistu et al., 2021). Satellite measurements may not detect all photosynthetic  
683 activity in tropical forests, including in the understory, mid-canopy, and the dense canopy.  
684 Differences in photosynthesis among these different levels can be key to estimating GPP  
685 and NBE of the entire forest; the canopy and understory can have very different seasonal  
686 dynamics in tropical forests, dynamics that may not be captured by satellite-based SIF.  
687 For example Tang and Dubayah (2017) find that leaf area index in the canopy and un-  
688 derstory are anti-correlated in tropical forests, and that dry season leaf loss from the canopy  
689 is associated with opportunistic leaf growth in the understory.

## 690 4 Conclusion

691 Remote sensing products like SIF and NIRv have shown enormous promise as pre-  
692 dictors of the global carbon cycle. Indeed, we find that existing SIF products are skilled  
693 at predicting variability in atmospheric CO<sub>2</sub> observations, and thus in predicting vari-  
694 ability in NBE, across the extra-tropics, particularly when compared to other vegeta-  
695 tion indicators and to state-of-the-art TBMs that do not assimilate SIF. Specifically, in-  
696 verse estimates of NBE that assimilate SIF products exhibit a different seasonal cycle,  
697 particularly during the fall months when CO<sub>2</sub> uptake by plants may decline more quickly  
698 than changes in vegetation greenness. However, we find that other vegetation indicators  
699 like NIRv, EVI, and NDVI are just as skilled at predicting patterns in CO<sub>2</sub> observations  
700 across large global biomes when we multiply these indicators by PAR, suggesting that  
701 NIRvP, EVIP, and NDVIP may, indeed, be reasonable structural proxies for SIF at global  
702 scales. By contrast, existing SIF products do not show the same advantage relative to  
703 other vegetation indicators in the tropics. Notably, the seasonal cycle of SIF products  
704 does not match inverse estimates of NBE nor does it match the seasonal cycle of TBMs  
705 that are skilled at predicting patterns in CO<sub>2</sub> observations from OCO-2. We are not able  
706 to reconcile this discrepancy using respiration estimates from the 15 TBMs analyzed in  
707 this study or using a biomass burning emissions estimate.

708 Overall, the results suggest that interpolated SIF products can be a powerful tool  
709 to improve bottom-up NBE estimates across the global extra-tropics. Specifically, the  
710 direct use of SIF within diagnostic TBMs (i.e., those that use forcing data or vegeta-  
711 tion characteristics from an external source) could improve the characterization of sea-  
712 sonal variability in GPP and NBE across the extra-tropics, while SIF could serve as an  
713 effective tool for evaluating or tuning seasonal variability of GPP in prognostic TBMs  
714 (i.e., those that calculate forcing data and vegetation characteristics internally). Indeed,  
715 several prognostic TBMs can be used to predict SIF, but these TBMs show wide disagree-  
716 ment on both SIF and GPP, at least at the site level Parazoo et al. (2020). However, this  
717 study suggests that there is more work to be done to understand the relationships be-

tween SIF, GPP, and NBE in the tropics. We argue that there is a need for more atmospheric CO<sub>2</sub> observations in the tropics that can be used to evaluate relationships between SIF, GPP, and NBE at intermediate regional scales. These include observations from aircraft or tall towers, as in Alden et al. (2016), and/or geostationary satellites like the Geostationary Carbon Cycle Observatory (GeoCarb). Such observations could help bridge the gap between site-level evaluation (e.g., Irteza et al., 2021; C. Wang et al., 2019; Doughty et al., 2019) and global-scale efforts like the present study.

## 5 Open Research

The atmospheric CO<sub>2</sub> observations from OCO-2 (b10, 10-second averages) and from the NOAA Obspack are publicly available from Baker (2021) and NOAA Global Monitoring Laboratory (2021), respectively. The SIF products are available from Yu et al. (2019a), Y. Zhang et al. (2018), and X. Li and Xiao (2019b); EVI and NDVI are available from NASA MODIS at (Didan, 2022), and the inputs required to calculate NIRv are also available from NASA MODIS (NASA, 2022). Furthermore, the meteorological variables used in this study, including PAR, are available from NASA at NASA Global Modeling and Assimilation Office (2019).

In addition, the inverse modeling simulations in this study use the code published in S. M. Miller and Saibaba (2019).

## Acknowledgments

We thank David Baker and Andrew Jacobson for providing the 10 s averaged OCO-2 and Obspack data files, respectively. We also thank Grayson Badgley for his help constructing NIRv and with the research more broadly. We further thank the research teams that generated the OCO-2 SIF products used in this study – led by Longlong Yu, and Yao Zhang. We also thank the Global Carbon Project TRENDY model team, including Stephen Sitch, Pierre Friedlingstein, Emilie Joetzjer, Vladislav Bastrikov, Daniel S. Goll, Vanessa Haverd, Atul K. Jain, Etsushi Kato, Sebastian Lienert, Danica L. Lombardozzi, Patrick C. McGuire, Joe R. Melton, Julia E. M. S. Nabel, Benjamin Poulter, Hanqin Tian, Andrew J. Wiltshire, and Sönke Zaehle. This work is funded by NASA grants 80NSSC18K0976 and 80NSSC21K1073. Jingfeng Xiao is supported by NSF (DEB-2017870).

## References

- Albright, R., Corbett, A., Jiang, X., Creecy, E., Newman, S., Li, K.-F., . . . Yung, Y. L. (2022). Seasonal variations of solar-induced fluorescence, precipitation, and carbon dioxide over the amazon. *Earth and Space Science*, 9(1), e2021EA002078. doi: 10.1029/2021EA002078
- Alden, C. B., Miller, J. B., Gatti, L. V., Gloor, M. M., Guan, K., Michalak, A. M., . . . Diffenbaugh, N. S. (2016). Regional atmospheric co<sub>2</sub> inversion reveals seasonal and geographic differences in amazon net biome exchange. *Global Change Biology*, 22(10), 3427-3443. Retrieved from <https://onlinelibrary.wiley.com/doi/abs/10.1111/gcb.13305> doi: 10.1111/gcb.13305
- Anav, A., Friedlingstein, P., Beer, C., Ciais, P., Harper, A., Jones, C., . . . Zhao, M. (2015). Spatiotemporal patterns of terrestrial gross primary production: A review. *Reviews of Geophysics*, 53(3), 785-818. doi: 10.1002/2015RG000483
- Bacour, C., Maignan, F., MacBean, N., Porcar-Castell, A., Flexas, J., Frankenberg, C., . . . Bastrikov, V. (2019). Improving estimates of gross primary productivity by assimilating solar-induced fluorescence satellite retrievals in a terrestrial biosphere model using a process-based SIF model. *Journal of Geophysical Research: Biogeosciences*, 124(11), 3281-3306. doi:

- 766 <https://doi.org/10.1029/2019JG005040>
- 767 Badgley, G., Anderegg, L. D. L., Berry, J. A., & Field, C. B. (2019). Terrestrial  
768 gross primary production: Using NIRv to scale from site to globe. *Global*  
769 *Change Biology*, 25(11), 3731-3740. doi: <https://doi.org/10.1111/gcb.14729>
- 770 Badgley, G., Field, C. B., & Berry, J. A. (2017). Canopy near-infrared reflectance  
771 and terrestrial photosynthesis. *Science Advances*, 3(3). doi: <https://doi.org/10.1126/sciadv.1602244>
- 772
- 773 Baker, D. F. (2021). *OCO-2 b10c 10sec* [dataset]. Retrieved 8 Feb. 2022, from  
774 [ftp.cira.colostate.edu:/ftp/BAKER/OC02\\_b10c\\_10sec\\_GOOD\\_r5.nc4](ftp.cira.colostate.edu:/ftp/BAKER/OC02_b10c_10sec_GOOD_r5.nc4) doi: 0.  
775 .1002/essoar.10505688.1
- 776 Bauerle, W. L., Oren, R., Way, D. A., Qian, S. S., Stoy, P. C., Thornton, P. E., ...  
777 Reynolds, R. F. (2012). Photoperiodic regulation of the seasonal pattern  
778 of photosynthetic capacity and the implications for carbon cycling. *Proceed-*  
779 *ings of the National Academy of Sciences*, 109(22), 8612-8617. Retrieved  
780 from <https://www.pnas.org/doi/abs/10.1073/pnas.1119131109> doi:  
781 10.1073/pnas.1119131109
- 782 Beer, C., Reichstein, M., Tomelleri, E., Ciais, P., Jung, M., Carvalhais, N., ...  
783 others (2010). Terrestrial gross carbon dioxide uptake: global distribu-  
784 tion and covariation with climate. *Science*, 329(5993), 834-838. doi:  
785 <https://doi.org/10.1126/science.1184984>
- 786 Byrne, B., Liu, J., Lee, M., Yin, Y., Bowman, K. W., Miyazaki, K., ... Paton-  
787 Walsh, C. (2021). The carbon cycle of southeast Australia during 2019–2020:  
788 Drought, fires, and subsequent recovery. *AGU Advances*, 2(4), e2021AV000469.  
789 Retrieved from [https://agupubs.onlinelibrary.wiley.com/doi/abs/](https://agupubs.onlinelibrary.wiley.com/doi/abs/10.1029/2021AV000469)  
790 [10.1029/2021AV000469](https://agupubs.onlinelibrary.wiley.com/doi/abs/10.1029/2021AV000469) (e2021AV000469 2021AV000469) doi: 10.1029/  
791 2021AV000469
- 792 Byrne, B., Wunch, D., Jones, D. B. A., Strong, K., Deng, F., Baker, I., ... Roehl,  
793 C. M. (2018). Evaluating GPP and respiration estimates over northern mid-  
794 latitude ecosystems using solar-induced fluorescence and atmospheric CO<sub>2</sub>  
795 measurements. *Journal of Geophysical Research: Biogeosciences*, 123(9),  
796 2976-2997. doi: 10.1029/2018JG004472
- 797 Carroll, D., Menemenlis, D., Adkins, J. F., Bowman, K. W., Brix, H., Dutkiewicz,  
798 S., ... Zhang, H. (2020). The ECCO-Darwin data-assimilative global ocean  
799 biogeochemistry model: Estimates of seasonal to multidecadal surface ocean  
800 pCO<sub>2</sub> and air-sea CO<sub>2</sub> flux. *Journal of Advances in Modeling Earth Systems*,  
801 12(10), e2019MS001888. doi: <https://doi.org/10.1029/2019MS001888>
- 802 Chang, Q., Xiao, X., Jiao, W., Wu, X., Doughty, R., Wang, J., ... Qin, Y. (2019).  
803 Assessing consistency of spring phenology of snow-covered forests as estimated  
804 by vegetation indices, gross primary production, and solar-induced chloro-  
805 phyll fluorescence. *Agricultural and Forest Meteorology*, 275, 305-316. doi:  
806 <https://doi.org/10.1016/j.agrformet.2019.06.002>
- 807 Chen, A., Mao, J., Ricciuto, D., Xiao, J., Frankenberg, C., Li, X., ... Knapp, A. K.  
808 (2021). Moisture availability mediates the relationship between terrestrial gross  
809 primary production and solar-induced chlorophyll fluorescence: Insights from  
810 global-scale variations. *Global Change Biology*, 27(6), 1144-1156. Retrieved  
811 from <https://onlinelibrary.wiley.com/doi/abs/10.1111/gcb.15373> doi:  
812 10.1111/gcb.15373
- 813 Chen, Z., Huntzinger, D. N., Liu, J., Piao, S., Wang, X., Sitch, S., ... Miller, S. M.  
814 (2021b). Five years of variability in the global carbon cycle: comparing an esti-  
815 mate from the Orbiting Carbon Observatory-2 and process-based models. *En-*  
816 *vironmental Research Letters*, 16(5), 054041. doi: 10.1088/1748-9326/abfac1
- 817 Chen, Z., Liu, J., Henze, D. K., Huntzinger, D. N., Wells, K. C., Sitch, S., ... Miller,  
818 S. M. (2021a). Linking global terrestrial CO<sub>2</sub> fluxes and environmental drivers:  
819 inferences from the Orbiting Carbon Observatory 2 satellite and terrestrial  
820 biospheric models. *Atmospheric Chemistry and Physics*, 21(9), 6663–6680. doi:

- 10.5194/acp-21-6663-2021
- 821  
822 Churkina, G., Schimel, D., Braswell, B. H., & Xiao, X. (2005). Spatial analy-  
823 sis of growing season length control over net ecosystem exchange. *Global*  
824 *Change Biology*, 11(10), 1777-1787. Retrieved from [https://onlinelibrary](https://onlinelibrary.wiley.com/doi/abs/10.1111/j.1365-2486.2005.001012.x)  
825 [.wiley.com/doi/abs/10.1111/j.1365-2486.2005.001012.x](https://onlinelibrary.wiley.com/doi/abs/10.1111/j.1365-2486.2005.001012.x) doi:  
826 10.1111/j.1365-2486.2005.001012.x
- 827 Damm, A., Guanter, L., Paul-Limoges, E., van der Tol, C., Hueni, A., Buchmann,  
828 N., ... Schaepman, M. (2015). Far-red sun-induced chlorophyll fluorescence  
829 shows ecosystem-specific relationships to gross primary production: An assess-  
830 ment based on observational and modeling approaches. *Remote Sensing of*  
831 *Environment*, 166, 91-105. doi: <https://doi.org/10.1016/j.rse.2015.06.004>
- 832 Dechant, B., Ryu, Y., Badgley, G., Köhler, P., Rascher, U., Migliavacca, M., ...  
833 Berry, J. A. (2022). Nirvp: A robust structural proxy for sun-induced chloro-  
834 phyll fluorescence and photosynthesis across scales. *Remote Sensing of Envi-*  
835 *ronment*, 268, 112763. doi: <https://doi.org/10.1016/j.rse.2021.112763>
- 836 Dechant, B., Ryu, Y., Badgley, G., Zeng, Y., Berry, J. A., Zhang, Y., ... Moya, I.  
837 (2020). Canopy structure explains the relationship between photosynthesis and  
838 sun-induced chlorophyll fluorescence in crops. *Remote Sensing of Environment*,  
839 241, 111733. Retrieved from [https://www.sciencedirect.com/science/](https://www.sciencedirect.com/science/article/pii/S0034425720301036)  
840 [article/pii/S0034425720301036](https://www.sciencedirect.com/science/article/pii/S0034425720301036) doi: 10.1016/j.rse.2020.111733
- 841 del Rosario Uribe, M., & Dukes, J. S. (2021, apr). Land cover change alters seasonal  
842 photosynthetic activity and transpiration of amazon forest and cerrado. *Envi-*  
843 *ronmental Research Letters*, 16(5), 054013. Retrieved from [https://doi.org/](https://doi.org/10.1088/1748-9326/abf60d)  
844 [10.1088/1748-9326/abf60d](https://doi.org/10.1088/1748-9326/abf60d) doi: 10.1088/1748-9326/abf60d
- 845 Didan, K. (2022). *MODIS Vegetation Index Products (NDVI and EVI)* [dataset].  
846 Retrieved 8 Feb. 2022, from [https://modis.gsfc.nasa.gov/data/dataproduct/](https://modis.gsfc.nasa.gov/data/dataproduct/mod13.php)  
847 [mod13.php](https://modis.gsfc.nasa.gov/data/dataproduct/mod13.php) doi: 10.5067/MODIS/MOD13C1.006
- 848 Ding, Y., Wang, F., Mu, Q., Sun, Y., Cai, H., Zhou, Z., ... Shi, H. (2021). Esti-  
849 mating land use/land cover change impacts on vegetation response to drought  
850 under 'grain for green' in the loess plateau. *Land Degradation & Development*,  
851 32(17), 5083-5098. Retrieved from [https://onlinelibrary.wiley.com/doi/](https://onlinelibrary.wiley.com/doi/abs/10.1002/ldr.4093)  
852 [abs/10.1002/ldr.4093](https://onlinelibrary.wiley.com/doi/abs/10.1002/ldr.4093) doi: 10.1002/ldr.4093
- 853 Doughty, R., Köhler, P., Frankenberg, C., Magney, T. S., Xiao, X., Qin, Y., ...  
854 Moore, B. (2019). Tropomi reveals dry-season increase of solar-induced chloro-  
855 phyll fluorescence in the amazon forest. *Proceedings of the National Academy*  
856 *of Sciences*, 116(44), 22393-22398. Retrieved from [https://www.pnas.org/](https://www.pnas.org/doi/abs/10.1073/pnas.1908157116)  
857 [doi/abs/10.1073/pnas.1908157116](https://www.pnas.org/doi/abs/10.1073/pnas.1908157116) doi: 10.1073/pnas.1908157116
- 858 Doughty, R., Xiao, X., Köhler, P., Frankenberg, C., Qin, Y., Wu, X., ... Moore III,  
859 B. (2021). Global-scale consistency of spaceborne vegetation indices, chloro-  
860 phyll fluorescence, and photosynthesis. *Journal of Geophysical Research:*  
861 *Biogeosciences*, 126(6), e2020JG006136. doi: [https://doi.org/10.1029/](https://doi.org/10.1029/2020JG006136)  
862 [2020JG006136](https://doi.org/10.1029/2020JG006136)
- 863 Fang, Y., & Michalak, A. M. (2015). Atmospheric observations inform CO<sub>2</sub> flux  
864 responses to enviroclimatic drivers. *Global Biogeochemical Cycles*, 29(5), 555-  
865 566. (2014GB005034) doi: <https://doi.org/10.1002/2014GB005034>
- 866 Fang, Y., Michalak, A. M., Shiga, Y. P., & Yadav, V. (2014). Using atmospheric  
867 observations to evaluate the spatiotemporal variability of CO<sub>2</sub> fluxes simu-  
868 lated by terrestrial biospheric models. *Biogeosciences*, 11(23), 6985-6997.  
869 Retrieved from <https://bg.copernicus.org/articles/11/6985/2014/> doi:  
870 10.5194/bg-11-6985-2014
- 871 Field, C. B., Randerson, J. T., & Malmström, C. M. (1995). Global net primary  
872 production: Combining ecology and remote sensing. *Remote Sensing of Envi-*  
873 *ronment*, 51(1), 74-88. (Remote Sensing of Land Surface for Studies of Global  
874 Change) doi: [https://doi.org/10.1016/0034-4257\(94\)00066-V](https://doi.org/10.1016/0034-4257(94)00066-V)
- 875 Frankenberg, C., Fisher, J. B., Worden, J., Badgley, G., Saatchi, S. S., Lee, J.-E.,

- 876 ... others (2011). New global observations of the terrestrial carbon cycle  
 877 from GOSAT: Patterns of plant fluorescence with gross primary productiv-  
 878 ity. *Geophysical Research Letters*, 38(17). doi: [https://doi.org/10.1029/](https://doi.org/10.1029/2011GL048738)  
 879 2011GL048738
- 880 Friedlingstein, P., Jones, M. W., O'Sullivan, M., Andrew, R. M., Hauck, J., Peters,  
 881 G. P., ... Zaehle, S. (2019). Global carbon budget 2019. *Earth System Science*  
 882 *Data*, 11(4), 1783–1838. doi: <https://doi.org/10.5194/essd-11-1783-2019>
- 883 Gelaro, R., McCarty, W., Suárez, M. J., Todling, R., Molod, A., Takacs, L., ...  
 884 Zhao, B. (2017). The modern-era retrospective analysis for research and  
 885 applications, version 2 (merra-2). *Journal of Climate*, 30(14), 5419 - 5454.  
 886 Retrieved from [https://journals.ametsoc.org/view/journals/clim/30/](https://journals.ametsoc.org/view/journals/clim/30/14/jcli-d-16-0758.1.xml)  
 887 14/jcli-d-16-0758.1.xml doi: 10.1175/JCLI-D-16-0758.1
- 888 Giglio, L., Randerson, J. T., & van der Werf, G. R. (2013). Analysis of daily,  
 889 monthly, and annual burned area using the fourth-generation global fire emis-  
 890 sions database (GFED4). *Journal of Geophysical Research: Biogeosciences*,  
 891 118(1), 317–328. doi: <https://doi.org/10.1002/jgrg.20042>
- 892 Goerner, A., Reichstein, M., & Rambal, S. (2009). Tracking seasonal drought  
 893 effects on ecosystem light use efficiency with satellite-based pri in a mediter-  
 894 ranean forest. *Remote Sensing of Environment*, 113(5), 1101-1111. Re-  
 895 trieved from [https://www.sciencedirect.com/science/article/pii/](https://www.sciencedirect.com/science/article/pii/S0034425709000285)  
 896 S0034425709000285 doi: 10.1016/j.rse.2009.02.001
- 897 Gonsamo, A., Chen, J. M., Price, D. T., Kurz, W. A., & Wu, C. (2012). Land  
 898 surface phenology from optical satellite measurement and CO<sub>2</sub> eddy covari-  
 899 ance technique. *Journal of Geophysical Research: Biogeosciences*, 117(G3).  
 900 Retrieved from [https://agupubs.onlinelibrary.wiley.com/doi/abs/](https://agupubs.onlinelibrary.wiley.com/doi/abs/10.1029/2012JG002070)  
 901 10.1029/2012JG002070 doi: 10.1029/2012JG002070
- 902 Gourdj, S. M., Mueller, K. L., Schaefer, K., & Michalak, A. M. (2008). Global  
 903 monthly averaged CO<sub>2</sub> fluxes recovered using a geostatistical inverse model-  
 904 ing approach: 2. results including auxiliary environmental data. *Journal of*  
 905 *Geophysical Research: Atmospheres*, 113(D21). Retrieved from [https://](https://agupubs.onlinelibrary.wiley.com/doi/abs/10.1029/2007JD009733)  
 906 [agupubs.onlinelibrary.wiley.com/doi/abs/10.1029/2007JD009733](https://agupubs.onlinelibrary.wiley.com/doi/abs/10.1029/2007JD009733) doi:  
 907 10.1029/2007JD009733
- 908 Gourdj, S. M., Mueller, K. L., Yadav, V., Huntzinger, D. N., Andrews, A. E.,  
 909 Trudeau, M., ... Michalak, A. M. (2012). North American CO<sub>2</sub> exchange:  
 910 inter-comparison of modeled estimates with results from a fine-scale atmo-  
 911 spheric inversion. *Biogeosciences*, 9(1), 457–475. doi: [https://doi.org/10.5194/](https://doi.org/10.5194/bg-9-457-2012)  
 912 bg-9-457-2012
- 913 Gu, L., Han, J., Wood, J. D., Chang, C. Y.-Y., & Sun, Y. (2019). Sun-induced  
 914 chl fluorescence and its importance for biophysical modeling of photosyn-  
 915 thesis based on light reactions. *New Phytologist*, 223(3), 1179–1191. doi:  
 916 <https://doi.org/10.1111/nph.15796>
- 917 Guan, K., Berry, J. A., Zhang, Y., Joiner, J., Guanter, L., Badgley, G., & Lobell,  
 918 D. B. (2016). Improving the monitoring of crop productivity using space-  
 919 borne solar-induced fluorescence. *Global Change Biology*, 22(2), 716-726. doi:  
 920 <https://doi.org/10.1111/gcb.13136>
- 921 Guan, K., Pan, M., Li, H., Wolf, A., Wu, J., Medvigy, D., ... Lyapustin, A. I.  
 922 (2015). Photosynthetic seasonality of global tropical forests constrained by  
 923 hydroclimate. *Nature Geoscience*, 8(4), 284–289. doi: [https://doi.org/10.1038/](https://doi.org/10.1038/ngeo2382)  
 924 ngeo2382
- 925 Guanter, L., Frankenberg, C., Dudhia, A., Lewis, P. E., Gómez-Dans, J., Kuze, A.,  
 926 ... Grainger, R. G. (2012). Retrieval and global assessment of terrestrial  
 927 chlorophyll fluorescence from gosat space measurements. *Remote Sensing of*  
 928 *Environment*, 121, 236-251. doi: <https://doi.org/10.1016/j.rse.2012.02.006>
- 929 Guanter, L., Zhang, Y., Jung, M., Joiner, J., Voigt, M., Berry, J. A., ... others  
 930 (2014). Global and time-resolved monitoring of crop photosynthesis with

- 931 chlorophyll fluorescence. *Proceedings of the National Academy of Sciences*,  
 932 *111*(14), E1327–E1333. doi: <https://doi.org/10.1073/pnas.1320008111>
- 933 He, M., Kimball, J. S., Yi, Y., Running, S., Guan, K., Jenco, K., . . . Maneta, M.  
 934 (2019, Jul). Impacts of the 2017 flash drought in the US northern plains in-  
 935 formed by satellite-based evapotranspiration and solar-induced fluorescence.  
 936 *Environmental Research Letters*, *14*(7), 074019. doi: [https://doi.org/10.1088/](https://doi.org/10.1088/1748-9326/ab22c3)  
 937 [1748-9326/ab22c3](https://doi.org/10.1088/1748-9326/ab22c3)
- 938 Helm, L. T., Shi, H., Lerda, M. T., & Yang, X. (2020). Solar-induced chlorophyll  
 939 fluorescence and short-term photosynthetic response to drought. *Ecological Ap-*  
 940 *plications*, *30*(5), e02101. doi: [10.1002/eap.2101](https://doi.org/10.1002/eap.2101)
- 941 Hu, J., Liu, L., Guo, J., Du, S., & Liu, X. (2018). Upscaling solar-induced chloro-  
 942 phyll fluorescence from an instantaneous to daily scale gives an improved  
 943 estimation of the gross primary productivity. *Remote Sensing*, *10*(10), 1663.  
 944 doi: <https://doi.org/10.3390/rs10101663>
- 945 Huntzinger, D., Michalak, A., Schwalm, C., Ciais, P., King, A., Fang, Y., . . . others  
 946 (2017). Uncertainty in the response of terrestrial carbon sink to environmental  
 947 drivers undermines carbon-climate feedback predictions. *Scientific reports*,  
 948 *7*(1), 1–8. doi: <https://doi.org/10.1038/s41598-017-03818-2>
- 949 Huntzinger, D., Post, W., Wei, Y., Michalak, A., West, T., Jacobson, A., . . . Cook,  
 950 R. (2012). North American Carbon Program (NACP) regional interim synthe-  
 951 sis: Terrestrial biospheric model intercomparison. *Ecological Modelling*, *232*,  
 952 144–157. doi: [10.1016/j.ecolmodel.2012.02.004](https://doi.org/10.1016/j.ecolmodel.2012.02.004)
- 953 Irteza, S. M., Nichol, J. E., Shi, W., & Abbas, S. (2021). Ndvi and fluorescence indi-  
 954 cators of seasonal and structural changes in a tropical forest succession. *Earth*  
 955 *Systems and Environment*, *5*(1), 127–133. doi: [10.1007/s41748-020-00175-5](https://doi.org/10.1007/s41748-020-00175-5)
- 956 Jacobson, A., Schuldt, K., Miller, J., Oda, T., Tans, P., Andrews, A., . . . Zimnoch,  
 957 M. (2020, May). *CarbonTracker documentation CT2019 release* [dataset].  
 958 Retrieved Dec. 29, 2021, from [https://gml.noaa.gov/ccgg/carbontracker/](https://gml.noaa.gov/ccgg/carbontracker/CT2019/CT2019_doc.php)  
 959 [CT2019/CT2019\\_doc.php](https://gml.noaa.gov/ccgg/carbontracker/CT2019/CT2019_doc.php) doi: <https://doi.org/10.25925/39m3-6069>
- 960 Jeong, S.-J., & Medvigy, D. (2014). Macroscale prediction of autumn leaf coloration  
 961 throughout the continental United States. *Global Ecology and Biogeography*,  
 962 *23*(11), 1245–1254. Retrieved from [https://onlinelibrary.wiley.com/doi/](https://onlinelibrary.wiley.com/doi/abs/10.1111/geb.12206)  
 963 [abs/10.1111/geb.12206](https://onlinelibrary.wiley.com/doi/abs/10.1111/geb.12206) doi: [10.1111/geb.12206](https://doi.org/10.1111/geb.12206)
- 964 Jeong, S.-J., Schimel, D., Frankenberg, C., Drewry, D. T., Fisher, J. B., Verma, M.,  
 965 . . . Joiner, J. (2017). Application of satellite solar-induced chlorophyll fluo-  
 966 rescence to understanding large-scale variations in vegetation phenology and  
 967 function over northern high latitude forests. *Remote Sensing of Environment*,  
 968 *190*, 178–187. Retrieved from [https://www.sciencedirect.com/science/](https://www.sciencedirect.com/science/article/pii/S0034425716304680)  
 969 [article/pii/S0034425716304680](https://www.sciencedirect.com/science/article/pii/S0034425716304680) doi: [10.1016/j.rse.2016.11.021](https://doi.org/10.1016/j.rse.2016.11.021)
- 970 Jiang, Z., Jones, D. B. A., Worden, H. M., Deeter, M. N., Henze, D. K., Worden,  
 971 J., . . . Schuck, T. J. (2013). Impact of model errors in convective trans-  
 972 port on co source estimates inferred from MOPITT CO retrievals. *Journal*  
 973 *of Geophysical Research: Atmospheres*, *118*(4), 2073–2083. Retrieved from  
 974 <https://agupubs.onlinelibrary.wiley.com/doi/abs/10.1002/jgrd.50216>  
 975 doi: [10.1002/jgrd.50216](https://doi.org/10.1002/jgrd.50216)
- 976 Jiao, W., Chang, Q., & Wang, L. (2019). The sensitivity of satellite solar-induced  
 977 chlorophyll fluorescence to meteorological drought. *Earth's Future*, *7*(5), 558–  
 978 573. doi: <https://doi.org/10.1029/2018EF001087>
- 979 Jung, M., Koirala, S., Weber, U., Ichii, K., Gans, F., Camps-Valls, G., . . . Reich-  
 980 stein, M. (2019). The FLUXCOM ensemble of global land-atmosphere energy  
 981 fluxes. *Scientific data*, *6*(1), 1–14. doi: [10.1038/s41597-019-0076-8](https://doi.org/10.1038/s41597-019-0076-8)
- 982 Jung, M., Schwalm, C., Migliavacca, M., Walther, S., Camps-Valls, G., Koirala, S.,  
 983 . . . Reichstein, M. (2020). Scaling carbon fluxes from eddy covariance sites to  
 984 globe: synthesis and evaluation of the FLUXCOM approach. *Biogeosciences*,  
 985 *17*(5), 1343–1365. Retrieved from <https://bg.copernicus.org/articles/>

- 17/1343/2020/ doi: 10.5194/bg-17-1343-2020
- 986 Kim, J., Ryu, Y., Dechant, B., Lee, H., Kim, H. S., Kornfeld, A., & Berry, J. A.  
987 (2021). Solar-induced chlorophyll fluorescence is non-linearly related to  
988 canopy photosynthesis in a temperate evergreen needleleaf forest during  
989 the fall transition. *Remote Sensing of Environment*, 258, 112362. doi:  
990 <https://doi.org/10.1016/j.rse.2021.112362>  
991
- 992 Kitanidis, P. K., & Vomvoris, E. G. (1983). A geostatistical approach to the inverse  
993 problem in groundwater modeling (steady state) and one-dimensional simu-  
994 lations. *Water Resour. Res.*, 19(3), 677-690. doi: [https://doi.org/10.1029/  
995 WR019i003p00677](https://doi.org/10.1029/WR019i003p00677)
- 996 Köhler, P., Frankenberg, C., Magney, T. S., Guanter, L., Joiner, J., & Landgraf,  
997 J. (2018). Global retrievals of solar-induced chlorophyll fluorescence with  
998 TROPOMI: First results and intersensor comparison to OCO-2. *Geo-  
999 physical Research Letters*, 45(19), 10–456. doi: [https://doi.org/10.1029/  
1000 2018GL079031](https://doi.org/10.1029/2018GL079031)
- 1001 Li, X., & Xiao, J. (2019a). A global, 0.05-degree product of solar-induced chlorophyll  
1002 fluorescence derived from OCO-2, MODIS, and reanalysis data. *Remote Sens-  
1003 ing*, 11(5). doi: 10.3390/rs11050517
- 1004 Li, X., & Xiao, J. (2019b). *GOSIF - global, OCO-2 based SIF product, v2* [dataset].  
1005 Global Ecology Data Repository. Retrieved 9 Sep. 2021, from [https://  
1006 globalecology.unh.edu/data/GOSIF.html](https://globalecology.unh.edu/data/GOSIF.html) doi: 10.3390/rs11050517
- 1007 Li, X., & Xiao, J. (2022). TROPOMI observations allow for robust exploration of  
1008 the relationship between solar-induced chlorophyll fluorescence and terrestrial  
1009 gross primary production. *Remote Sensing of Environment*, 268, 112748. doi:  
1010 <https://doi.org/10.1016/j.rse.2021.112748>
- 1011 Li, X., Xiao, J., & He, B. (2018). Chlorophyll fluorescence observed by OCO-2  
1012 is strongly related to gross primary productivity estimated from flux towers  
1013 in temperate forests. *Remote Sensing of Environment*, 204, 659-671. doi:  
1014 <https://doi.org/10.1016/j.rse.2017.09.034>
- 1015 Li, X., Xiao, J., He, B., Arain, M. A., Beringer, J., Desai, A. R., ... others (2018).  
1016 Solar-induced chlorophyll fluorescence is strongly correlated with terrestrial  
1017 photosynthesis for a wide variety of biomes: First global analysis based on  
1018 OCO-2 and flux tower observations. *Global change biology*, 24(9), 3990–4008.  
1019 doi: <https://doi.org/10.1111/gcb.14297>
- 1020 Li, Z., Zhang, Q., Li, J., Yang, X., Wu, Y., Zhang, Z., ... Zhang, Y. (2020). Solar-  
1021 induced chlorophyll fluorescence and its link to canopy photosynthesis in maize  
1022 from continuous ground measurements. *Remote Sensing of Environment*, 236,  
1023 111420. doi: <https://doi.org/10.1016/j.rse.2019.111420>
- 1024 Liu, J., Bowman, K. W., Schimel, D. S., Parazoo, N. C., Jiang, Z., Lee, M., ...  
1025 Elderling, A. (2017). Contrasting carbon cycle responses of the tropical con-  
1026 tinents to the 2015–2016 El Niño. *Science*, 358(6360), eaam5690. Retrieved  
1027 from <https://www.science.org/doi/abs/10.1126/science.aam5690> doi:  
1028 10.1126/science.aam5690
- 1029 Liu, J., Wennberg, P. O., Parazoo, N. C., Yin, Y., & Frankenberg, C. (2020). Ob-  
1030 servational constraints on the response of high-latitude northern forests to  
1031 warming. *AGU Advances*, 1(4), e2020AV000228. Retrieved from [https://  
1032 agupubs.onlinelibrary.wiley.com/doi/abs/10.1029/2020AV000228](https://agupubs.onlinelibrary.wiley.com/doi/abs/10.1029/2020AV000228)  
1033 (e2020AV000228 2020AV000228) doi: 10.1029/2020AV000228
- 1034 Luus, K. A., Commane, R., Parazoo, N. C., Benmergui, J., Euskirchen, E. S.,  
1035 Frankenberg, C., ... Lin, J. C. (2017). Tundra photosynthesis captured by  
1036 satellite-observed solar-induced chlorophyll fluorescence. *Geophysical Research  
1037 Letters*, 44(3), 1564-1573. doi: 10.1002/2016GL070842
- 1038 Ma, X., Huete, A., Yu, Q., Restrepo-Coupe, N., Beringer, J., Hutley, L. B., ... Ea-  
1039 mus, D. (2014). Parameterization of an ecosystem light-use-efficiency model for  
1040 predicting savanna GPP using MODIS EVI. *Remote Sensing of Environment*,

- 1041 154, 253-271. Retrieved from [https://www.sciencedirect.com/science/](https://www.sciencedirect.com/science/article/pii/S0034425714003228)  
 1042 [article/pii/S0034425714003228](https://www.sciencedirect.com/science/article/pii/S0034425714003228) doi: 10.1016/j.rse.2014.08.025
- 1043 MacBean, N., Maignan, F., Bacour, C., Lewis, P., Peylin, P., Guanter, L., ... Dis-  
 1044 ney, M. (2018). Strong constraint on modelled global carbon uptake using  
 1045 solar-induced chlorophyll fluorescence data. *Scientific reports*, 8(1), 1–12. doi:  
 1046 <https://doi.org/10.1038/s41598-018-20024-w>
- 1047 Madani, N., Parazoo, N. C., & Miller, C. E. (2022). Climate change is enforcing  
 1048 physiological changes in arctic ecosystems. *Nature Communications Earth &*  
 1049 *Environment*, 0(0), in review.
- 1050 Magney, T. S., Barnes, M. L., & Yang, X. (2020). On the covariation of chloro-  
 1051 phyll fluorescence and photosynthesis across scales. *Geophysical Research Let-*  
 1052 *ters*, 47(23), e2020GL091098. doi: 10.1029/2020GL091098
- 1053 Magney, T. S., Bowling, D. R., Logan, B. A., Grossmann, K., Stutz, J., Blanken,  
 1054 P. D., ... Frankenberg, C. (2019). Mechanistic evidence for tracking  
 1055 the seasonality of photosynthesis with solar-induced fluorescence. *Pro-*  
 1056 *ceedings of the National Academy of Sciences*, 116(24), 11640-11645. doi:  
 1057 10.1073/pnas.1900278116
- 1058 Magney, T. S., Frankenberg, C., Fisher, J. B., Sun, Y., North, G. B., Davis,  
 1059 T. S., ... Siebke, K. (2017). Connecting active to passive fluorescence  
 1060 with photosynthesis: A method for evaluating remote sensing measure-  
 1061 ments of chl fluorescence. *New phytologist*, 215(4), 1594–1608. doi:  
 1062 <https://doi.org/10.1111/nph.14662>
- 1063 Magney, T. S., Frankenberg, C., Köhler, P., North, G., Davis, T. S., Dold, C.,  
 1064 ... others (2019). Disentangling changes in the spectral shape of chloro-  
 1065 phyll fluorescence: Implications for remote sensing of photosynthesis. *Jour-*  
 1066 *nal of Geophysical Research: Biogeosciences*, 124(6), 1491–1507. doi:  
 1067 10.1029/2019JG005029
- 1068 Mahadevan, P., Wofsy, S. C., Matross, D. M., Xiao, X., Dunn, A. L., Lin, J. C.,  
 1069 ... Gottlieb, E. W. (2008). A satellite-based biosphere parameterization  
 1070 for net ecosystem CO<sub>2</sub> exchange: Vegetation photosynthesis and respira-  
 1071 tion model (VPRM). *Global Biogeochemical Cycles*, 22(2), GB2005. doi:  
 1072 <https://doi.org/10.1029/2006GB002735>
- 1073 Marrs, J. K., Reblin, J. S., Logan, B. A., Allen, D. W., Reinmann, A. B., Bom-  
 1074 bard, D. M., ... Hutyrá, L. R. (2020). Solar-induced fluorescence does not  
 1075 track photosynthetic carbon assimilation following induced stomatal closure.  
 1076 *Geophysical Research Letters*, 47(15), e2020GL087956. (e2020GL087956  
 1077 2020GL087956) doi: <https://doi.org/10.1029/2020GL087956>
- 1078 Mengistu, A. G., Mengistu Tsidu, G., Koren, G., Kooreman, M. L., Boersma,  
 1079 K. F., Tagesson, T., ... Peters, W. (2021). Sun-induced fluorescence and  
 1080 near-infrared reflectance of vegetation track the seasonal dynamics of gross  
 1081 primary production over africa. *Biogeosciences*, 18(9), 2843–2857. Re-  
 1082 trieved from <https://bg.copernicus.org/articles/18/2843/2021/> doi:  
 1083 10.5194/bg-18-2843-2021
- 1084 Meroni, M., Rossini, M., Guanter, L., Alonso, L., Rascher, U., Colombo, R., &  
 1085 Moreno, J. (2009). Remote sensing of solar-induced chlorophyll fluores-  
 1086 cence: Review of methods and applications. *Remote Sensing of Environment*,  
 1087 113(10), 2037-2051. doi: 10.1016/j.rse.2009.05.003
- 1088 Michalak, A. M., Bruhwiler, L., & Tans, P. P. (2004). A geostatistical approach to  
 1089 surface flux estimation of atmospheric trace gases. *Journal of Geophysical Re-*  
 1090 *search: Atmospheres*, 109(D14). doi: <https://doi.org/10.1029/2003JD004422>
- 1091 Miller, S., Worthy, D. J., Michalak, A., Wofsy, S., Kort, E., Havice, T., ... Zhang,  
 1092 B. (2014a). Observational constraints on the distribution, seasonality, and  
 1093 environmental predictors of north american boreal methane emissions. *Global*  
 1094 *Biogeochemical Cycles*, 28(2), 146-160. doi: 10.1002/2013GB004580
- 1095 Miller, S. M., Matross, D. M., Andrews, A. E., Millet, D. B., Longo, M., Got-

- 1096 tlieb, E. W., . . . Wofsy, S. C. (2008). Sources of carbon monoxide and  
 1097 formaldehyde in North America determined from high-resolution atmo-  
 1098 spheric data. *Atmospheric Chemistry and Physics*, 8(24), 7673–7696. Re-  
 1099 trieved from <https://acp.copernicus.org/articles/8/7673/2008/> doi:  
 1100 10.5194/acp-8-7673-2008
- 1101 Miller, S. M., & Michalak, A. M. (2020b). The impact of improved satellite re-  
 1102 trievals on estimates of biospheric carbon balance. *Atmospheric Chemistry and*  
 1103 *Physics*, 20(1), 323–331. doi: 10.5194/acp-20-323-2020
- 1104 Miller, S. M., Michalak, A. M., Yadav, V., & Tadić, J. M. (2018). Character-  
 1105 izing biospheric carbon balance using CO<sub>2</sub> observations from the OCO-  
 1106 2 satellite. *Atmospheric Chemistry and Physics*, 18(9), 6785–6799. doi:  
 1107 10.5194/acp-18-6785-2018
- 1108 Miller, S. M., Miller, C. E., Commane, R., Chang, R. Y., Dinardo, S. J., Henderson,  
 1109 J. M., . . . Michalak, A. M. (2016a). A multiyear estimate of methane fluxes  
 1110 in alaska from carve atmospheric observations. *Global Biogeochemical Cycles*,  
 1111 30(10), 1441–1453. doi: 10.1002/2016GB005419
- 1112 Miller, S. M., & Saibaba, A. (2019). *Geostatistical inverse modeling with large atmo-*  
 1113 *spheric datasets*. Zenodo. doi: 10.5281/zenodo.3595574
- 1114 Miller, S. M., Saibaba, A. K., Trudeau, M. E., Mountain, M. E., & Andrews, A. E.  
 1115 (2020a). Geostatistical inverse modeling with very large datasets: an exam-  
 1116 ple from the Orbiting Carbon Observatory 2 (OCO-2) satellite. *Geoscientific*  
 1117 *Model Development*, 13(3), 1771–1785. doi: 10.5194/gmd-13-1771-2020
- 1118 NASA. (2000). *Normalized difference vegetation index (ndvi)*. Retrieved  
 1119 15 July 2022, from [https://earthobservatory.nasa.gov/features/](https://earthobservatory.nasa.gov/features/MeasuringVegetation/measuring_vegetation_2.php)  
 1120 [MeasuringVegetation/measuring\\_vegetation\\_2.php](https://earthobservatory.nasa.gov/features/MeasuringVegetation/measuring_vegetation_2.php)
- 1121 NASA. (2022). *MCD43C3 - MODIS/Terra+Aqua albedo 16-day L3 global 0.05deg*  
 1122 *CMG* [dataset]. Retrieved 8 Feb. 2022, from [https://ladsweb.modaps](https://ladsweb.modaps.eosdis.nasa.gov/missions-and-measurements/products/MCD43C3/)  
 1123 [.eosdis.nasa.gov/missions-and-measurements/products/MCD43C3/](https://ladsweb.modaps.eosdis.nasa.gov/missions-and-measurements/products/MCD43C3/) doi:  
 1124 10.5067/MODIS/MCD43C3.006
- 1125 NASA Global Modeling and Assimilation Office. (2019). *Modern-Era Retrospec-*  
 1126 *tive analysis for Research and Applications, version 2* [dataset]. Retrieved 8  
 1127 Feb. 2022, from <https://gmao.gsfc.nasa.gov/reanalysis/MERRA-2/> doi:  
 1128 10.5067/L0T5GEG1NYFA
- 1129 NOAA Global Monitoring Laboratory. (2021). *Observation package (ObsPack) data*  
 1130 *products, v3.2* [dataset]. Retrieved Dec. 29, 2021, from [https://gml.noaa](https://gml.noaa.gov/ccgg/obspack/data.php?id=obspack_co2_1_OC02MIP_v3.2_2021-05-20)  
 1131 [.gov/ccgg/obspack/data.php?id=obspack\\_co2\\_1\\_OC02MIP\\_v3.2\\_2021-05-20](https://gml.noaa.gov/ccgg/obspack/data.php?id=obspack_co2_1_OC02MIP_v3.2_2021-05-20)  
 1132 doi: <https://doi.org/10.25925/20210519>
- 1133 Oda, T., Maksyutov, S., & Andres, R. J. (2018). The Open-source Data Inventory  
 1134 for Anthropogenic CO<sub>2</sub>, version 2016 (ODIAC2016): a global monthly fos-  
 1135 sil fuel CO<sub>2</sub> gridded emissions data product for tracer transport simulations  
 1136 and surface flux inversions. *Earth System Science Data*, 10(1), 87–107. doi:  
 1137 <https://doi.org/10.5194/essd-10-87-2018>
- 1138 Parazoo, N. C., Bowman, K., Frankenberg, C., Lee, J.-E., Fisher, J. B., Worden, J.,  
 1139 . . . Gerbig, C. (2013). Interpreting seasonal changes in the carbon balance  
 1140 of southern amazonia using measurements of XCO<sub>2</sub> and chlorophyll fluores-  
 1141 cence from gosat. *Geophysical Research Letters*, 40(11), 2829–2833. doi:  
 1142 10.1002/grl.50452
- 1143 Parazoo, N. C., Magney, T., Norton, A., Raczka, B., Bacour, C., Maignan, F.,  
 1144 . . . Frankenberg, C. (2020). Wide discrepancies in the magnitude and  
 1145 direction of modeled solar-induced chlorophyll fluorescence in response  
 1146 to light conditions. *Biogeosciences*, 17(13), 3733–3755. Retrieved from  
 1147 <https://bg.copernicus.org/articles/17/3733/2020/> doi: 10.5194/  
 1148 bg-17-3733-2020
- 1149 Peiro, H., Crowell, S., Schuh, A., Baker, D. F., O’Dell, C., Jacobson, A. R., . . .  
 1150 Baker, I. (2022). Four years of global carbon cycle observed from the orbiting

- 1151 carbon observatory 2 (OCO-2) version 9 and in situ data and comparison to  
 1152 OCO-2 version 7. *Atmospheric Chemistry and Physics*, 22(2), 1097–1130. Re-  
 1153 trieved from <https://acp.copernicus.org/articles/22/1097/2022/> doi:  
 1154 10.5194/acp-22-1097-2022
- 1155 Pierrat, Z., Magney, T., Parazoo, N. C., Grossmann, K., Bowling, D. R., Seibt,  
 1156 U., ... Stutz, J. (2022). Diurnal and seasonal dynamics of solar-induced  
 1157 chlorophyll fluorescence, vegetation indices, and gross primary productivity in  
 1158 the boreal forest. *Journal of Geophysical Research: Biogeosciences*, 127(2),  
 1159 e2021JG006588. Retrieved from [https://agupubs.onlinelibrary.wiley](https://agupubs.onlinelibrary.wiley.com/doi/abs/10.1029/2021JG006588)  
 1160 [.com/doi/abs/10.1029/2021JG006588](https://agupubs.onlinelibrary.wiley.com/doi/abs/10.1029/2021JG006588) (e2021JG006588 2021JG006588) doi:  
 1161 10.1029/2021JG006588
- 1162 Pierrat, Z., Nehemy, M. F., Roy, A., Magney, T., Parazoo, N. C., Laroque, C., ...  
 1163 Stutz, J. (2021). Tower-based remote sensing reveals mechanisms behind  
 1164 a two-phased spring transition in a mixed-species boreal forest. *Journal of*  
 1165 *Geophysical Research: Biogeosciences*, 126(5), e2020JG006191. Retrieved  
 1166 from [https://agupubs.onlinelibrary.wiley.com/doi/abs/10.1029/](https://agupubs.onlinelibrary.wiley.com/doi/abs/10.1029/2020JG006191)  
 1167 [2020JG006191](https://agupubs.onlinelibrary.wiley.com/doi/abs/10.1029/2020JG006191) (e2020JG006191 2020JG006191) doi: 10.1029/2020JG006191
- 1168 Saibaba, A. K., & Kitanidis, P. K. (2015). Fast computation of uncertainty quan-  
 1169 tification measures in the geostatistical approach to solve inverse problems.  
 1170 *Advances in Water Resources*, 82(0), 124-138. doi: [https://doi.org/10.1016/](https://doi.org/10.1016/j.advwatres.2015.04.012)  
 1171 [j.advwatres.2015.04.012](https://doi.org/10.1016/j.advwatres.2015.04.012)
- 1172 Schwarz, G. (1978). Estimating the dimension of a model. *The Annals of Statistics*,  
 1173 6(2), 461 – 464. doi: <https://doi.org/10.1214/aos/1176344136>
- 1174 Schwarz, P. A., Law, B. E., Williams, M., Irvine, J., Kurpius, M., & Moore, D.  
 1175 (2004). Climatic versus biotic constraints on carbon and water fluxes in sea-  
 1176 sonally drought-affected ponderosa pine ecosystems. *Global Biogeochemical*  
 1177 *Cycles*, 18(4). Retrieved from [https://agupubs.onlinelibrary.wiley.com/](https://agupubs.onlinelibrary.wiley.com/doi/abs/10.1029/2004GB002234)  
 1178 [doi/abs/10.1029/2004GB002234](https://agupubs.onlinelibrary.wiley.com/doi/abs/10.1029/2004GB002234) doi: 10.1029/2004GB002234
- 1179 Shekhar, A., Chen, J., Bhattacharjee, S., Buras, A., Castro, A. O., Zang, C. S., &  
 1180 Rammig, A. (2020). Capturing the impact of the 2018 european drought and  
 1181 heat across different vegetation types using OCO-2 solar-induced fluorescence.  
 1182 *Remote Sensing*, 12(19). doi: <https://doi.org/10.3390/rs12193249>
- 1183 Shiga, Y. P., Michalak, A. M., Fang, Y., Schaefer, K., Andrews, A. E., Huntzinger,  
 1184 D. H., ... Wei, Y. (2018a). Forests dominate the interannual variability of  
 1185 the North American carbon sink. *Environ. Res. Lett.*, 13(8), 084015. doi:  
 1186 <https://doi.org/10.1088/1748-9326/aad505>
- 1187 Shiga, Y. P., Michalak, A. M., Fang, Y., Schaefer, K., Andrews, A. E., Huntzinger,  
 1188 D. H., ... Wei, Y. (2018b, aug). Forests dominate the interannual variability  
 1189 of the North American carbon sink. *Environmental Research Letters*, 13(8),  
 1190 084015. doi: 10.1088/1748-9326/aad505
- 1191 Sitch, S., Friedlingstein, P., Gruber, N., Jones, S. D., Murray-Tortarolo, G.,  
 1192 Ahlstrom, A., ... Myneni, R. (2015). Recent trends and drivers of regional  
 1193 sources and sinks of carbon dioxide. *Biogeosciences*, 12(3), 653–679. doi:  
 1194 <https://doi.org/10.5194/bg-12-653-2015>
- 1195 Sun, W., Fang, Y., Luo, X., Shiga, Y. P., Zhang, Y., Andrews, A. E., ... Micha-  
 1196 lak, A. M. (2021). Midwest US croplands determine model divergence in  
 1197 North American carbon fluxes. *AGU Advances*, 2(2), e2020AV000310. doi:  
 1198 [10.1029/2020AV000310](https://doi.org/10.1029/2020AV000310)
- 1199 Sun, Y., Frankenberg, C., Jung, M., Joiner, J., Guanter, L., Köhler, P., & Magney,  
 1200 T. (2018). Overview of solar-induced chlorophyll fluorescence (SIF) from  
 1201 the Orbiting Carbon Observatory-2: Retrieval, cross-mission comparison, and  
 1202 global monitoring for GPP. *Remote Sensing of Environment*, 209, 808-823.  
 1203 doi: <https://doi.org/10.1016/j.rse.2018.02.016>
- 1204 Tang, H., & Dubayah, R. (2017). Light-driven growth in amazon evergreen  
 1205 forests explained by seasonal variations of vertical canopy structure. *Pro-*

- 1206 *ceedings of the National Academy of Sciences*, 114(10), 2640-2644. doi:  
 1207 <https://doi.org/10.1073/pnas.1616943114>
- 1208 Thum, T., Zaehle, S., Köhler, P., Aalto, T., Aurela, M., Guanter, L., ... Markkanen,  
 1209 T. (2017). Modelling sun-induced fluorescence and photosynthesis with a land  
 1210 surface model at local and regional scales in northern europe. *Biogeosciences*,  
 1211 14(7), 1969–1987. doi: <https://doi.org/10.5194/bg-14-1969-2017>
- 1212 USGS. (2022). *Landsat enhanced vegetation index*. Retrieved 15 July 2022, from  
 1213 <https://www.usgs.gov/landsat-missions/landsat-enhanced-vegetation>  
 1214 [-index#:~:text=Landsat%20Enhanced%20Vegetation%20Index%20\(EVI,in%20areas%20with%20dense%20vegetation.](https://www.usgs.gov/landsat-missions/landsat-enhanced-vegetation)
- 1216 Verma, M., Schimel, D., Evans, B., Frankenberg, C., Beringer, J., Drewry, D., ...  
 1217 Eldering, A. (2017). Effect of environmental conditions on the relationship  
 1218 between solar-induced fluorescence and gross primary productivity at an ozflux  
 1219 grassland site. *Journal of Geophysical Research: Biogeosciences*, 122. doi:  
 1220 <https://doi.org/10.1002/2016JG003580>
- 1221 Walther, S., Voigt, M., Thum, T., Gonsamo, A., Zhang, Y., Köhler, P., ... Guanter,  
 1222 L. (2016). Satellite chlorophyll fluorescence measurements reveal large-  
 1223 scale decoupling of photosynthesis and greenness dynamics in boreal ever-  
 1224 green forests. *Global Change Biology*, 22(9), 2979-2996. Retrieved from  
 1225 <https://onlinelibrary.wiley.com/doi/abs/10.1111/gcb.13200> doi:  
 1226 10.1111/gcb.13200
- 1227 Wang, C., Beringer, J., Hutley, L. B., Cleverly, J., Li, J., Liu, Q., & Sun, Y. (2019).  
 1228 Phenology dynamics of dryland ecosystems along the north Australian tropical  
 1229 transect revealed by satellite solar-induced chlorophyll fluorescence. *Geo-*  
 1230 *physical Research Letters*, 46(10), 5294-5302. Retrieved from [https://](https://agupubs.onlinelibrary.wiley.com/doi/abs/10.1029/2019GL082716)  
 1231 [agupubs.onlinelibrary.wiley.com/doi/abs/10.1029/2019GL082716](https://agupubs.onlinelibrary.wiley.com/doi/abs/10.1029/2019GL082716) doi:  
 1232 10.1029/2019GL082716
- 1233 Wang, F., Chen, B., Lin, X., & Zhang, H. (2020). Solar-induced chlorophyll fluores-  
 1234 cence as an indicator for determining the end date of the vegetation growing  
 1235 season. *Ecological Indicators*, 109, 105755. doi: [https://doi.org/10.1016/](https://doi.org/10.1016/j.ecolind.2019.105755)  
 1236 [j.ecolind.2019.105755](https://doi.org/10.1016/j.ecolind.2019.105755)
- 1237 Wang, S., Zhang, Y., Ju, W., Qiu, B., & Zhang, Z. (2021). Tracking the seasonal  
 1238 and inter-annual variations of global gross primary production during last four  
 1239 decades using satellite near-infrared reflectance data. *Science of The Total En-*  
 1240 *vironment*, 755, 142569. doi: <https://doi.org/10.1016/j.scitotenv.2020.142569>
- 1241 Wen, J., Köhler, P., Duveiller, G., Parazoo, N., Magney, T., Hooker, G., ... Sun,  
 1242 Y. (2020). A framework for harmonizing multiple satellite instruments  
 1243 to generate a long-term global high spatial-resolution solar-induced chloro-  
 1244 phyll fluorescence (SIF). *Remote Sensing of Environment*, 239, 111644. doi:  
 1245 <https://doi.org/10.1016/j.rse.2020.111644>
- 1246 Wood, J. D., Griffis, T. J., Baker, J. M., Frankenberg, C., Verma, M., & Yuen,  
 1247 K. (2017). Multiscale analyses of solar-induced fluorescence and gross pri-  
 1248 mary production. *Geophysical Research Letters*, 44(1), 533–541. doi:  
 1249 <https://doi.org/10.1002/2016GL070775>
- 1250 Yang, X., Tang, J., Mustard, J. F., Lee, J.-E., Rossini, M., Joiner, J., ... Richard-  
 1251 son, A. D. (2015). Solar-induced chlorophyll fluorescence that correlates  
 1252 with canopy photosynthesis on diurnal and seasonal scales in a temper-  
 1253 ate deciduous forest. *Geophysical Research Letters*, 42(8), 2977-2987. doi:  
 1254 <https://doi.org/10.1002/2015GL063201>
- 1255 Yu, L., Wen, J., Chang, C. Y., Frankenberg, C., & Sun, Y. (2019a). *High reso-*  
 1256 *lution global contiguous SIF estimates derived from OCO-2 SIF and MODIS*  
 1257 [dataset]. ORNL Distributed Active Archive Center. Retrieved 9 Sep. 2021,  
 1258 from [https://daac.ornl.gov/cgi-bin/dsviewer.pl?ds\\_id=1696](https://daac.ornl.gov/cgi-bin/dsviewer.pl?ds_id=1696) doi:  
 1259 10.3334/ORNLDAAC/1696
- 1260 Yu, L., Wen, J., Chang, C. Y., Frankenberg, C., & Sun, Y. (2019b). High-resolution

- 1261 global contiguous SIF of OCO-2. *Geophysical Research Letters*, 46(3), 1449-  
1262 1458. doi: 10.1029/2018GL081109
- 1263 Zeng, Y., Badgley, G., Dechant, B., Ryu, Y., Chen, M., & Berry, J. (2019). A prac-  
1264 tical approach for estimating the escape ratio of near-infrared solar-induced  
1265 chlorophyll fluorescence. *Remote Sensing of Environment*, 232, 111209. Re-  
1266 trieved from [https://www.sciencedirect.com/science/article/pii/](https://www.sciencedirect.com/science/article/pii/S0034425719302226)  
1267 [S0034425719302226](https://www.sciencedirect.com/science/article/pii/S0034425719302226) doi: 10.1016/j.rse.2019.05.028
- 1268 Zhang, J., Xiao, J., Tong, X., Zhang, J., Meng, P., Li, J., ... Yu, P. (2022). NIRv  
1269 and SIF better estimate phenology than NDVI and EVI: Effects of spring and  
1270 autumn phenology on ecosystem production of planted forests. *Agricultural*  
1271 *and Forest Meteorology*, 315, 108819. doi: 10.1016/j.agrformet.2022.108819
- 1272 Zhang, L., Qiao, N., Huang, C., & Wang, S. (2019). Monitoring drought effects on  
1273 vegetation productivity using satellite solar-induced chlorophyll fluorescence.  
1274 *Remote Sensing*, 11(4). doi: <https://doi.org/10.3390/rs11040378>
- 1275 Zhang, Y., Commane, R., Zhou, S., Williams, A. P., & Gentine, P. (2020). Light  
1276 limitation regulates the response of autumn terrestrial carbon uptake to warm-  
1277 ing. *Nature Climate Change*, 10(8), 739–743. doi: 10.1038/s41558-020-0806-0
- 1278 Zhang, Y., Joiner, J., Alemohammad, S. H., Zhou, S., & Gentine, P. (2018). A  
1279 global spatially contiguous solar-induced fluorescence (CSIF) dataset us-  
1280 ing neural networks. *Biogeosciences*, 15(19), 5779–5800. doi: 10.5194/  
1281 bg-15-5779-2018
- 1282 Zuromski, L. M., Bowling, D. R., Köhler, P., Frankenberg, C., Goulden, M. L.,  
1283 Blanken, P. D., & Lin, J. C. (2018). Solar-induced fluorescence detects in-  
1284 terannual variation in gross primary production of coniferous forests in the  
1285 western united states. *Geophysical Research Letters*, 45(14), 7184-7193. doi:  
1286 <https://doi.org/10.1029/2018GL077906>

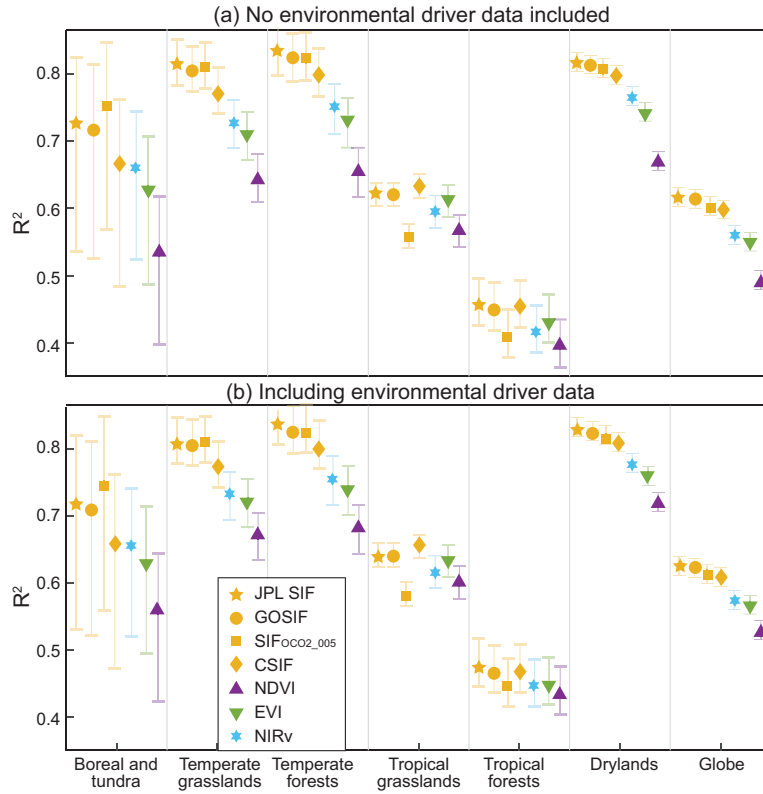


**Figure 1.** Results from the linear model using vegetation indicators as predictor variables (a) and using vegetation indicators plus environmental driver variables (b). This figure specifically shows the linear model fit ( $R^2$ ) when compared against  $\text{CO}_2$  observations from OCO-2. Overall, we find that SIF products yield a better model-data fit ( $R^2$ ) compared to other vegetation indicators across the extra-tropics, but SIF products do not exhibit the same advantage in the tropics. We also find that the inclusion of additional predictor variables to help better describe variability in NBE (panel b) does not substantially improve or otherwise change the model-data fit. Note that we combine boreal and tundra biomes for OCO-2 simulations, due to the paucity of OCO-2 observations over the tundra.

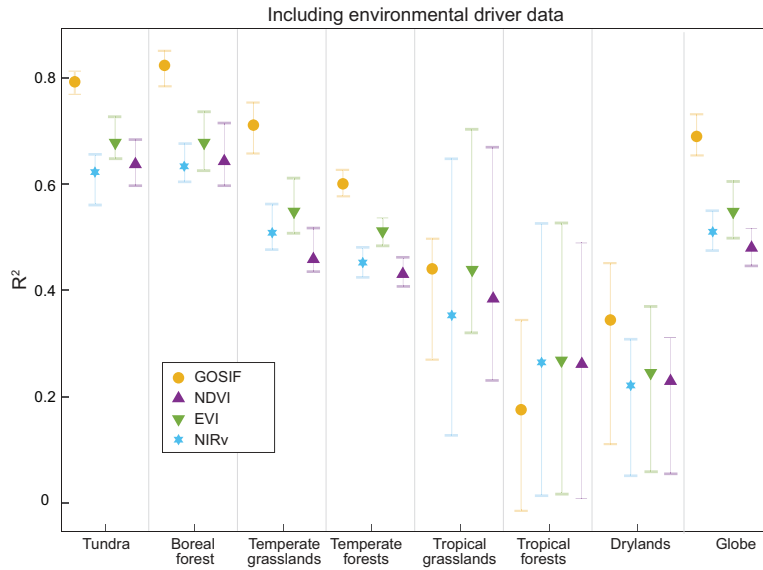


**Figure 2.** Results from the linear model using in situ CO<sub>2</sub> observations instead of CO<sub>2</sub> observations from OCO-2. The linear model results using in situ CO<sub>2</sub> observations broadly parallel results using OCO-2 observations. Notably, a linear model using GOSIF yields a better fit to in situ CO<sub>2</sub> observations than other vegetation indicators, at least in the extra-tropics.

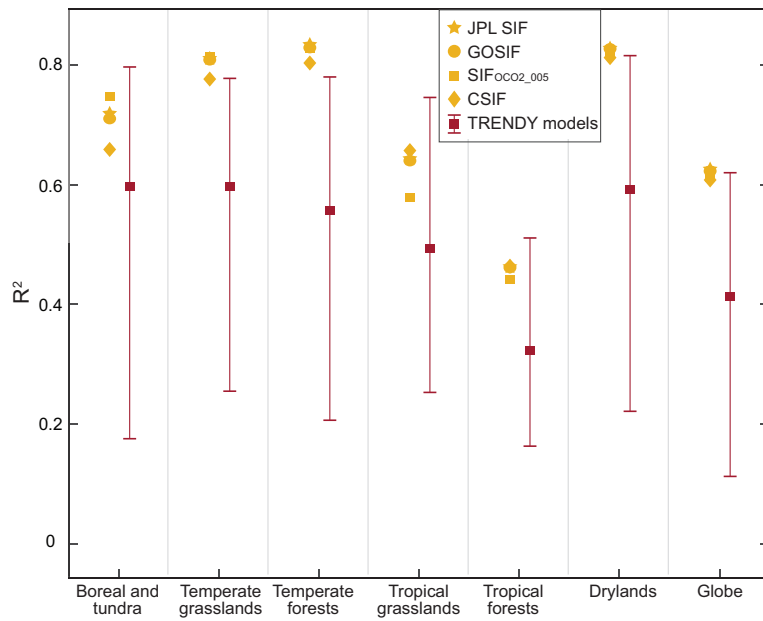


**Figure 3.** A comparison between the SIF-based linear model and NBE estimates from 15 bottom-up models in TRENDY. This figure displays the model-data fit ( $R^2$ ) of the linear model and TRENDY models against CO<sub>2</sub> observations from OCO-2. In several biomes (temperate grasslands, temperate forests, and drylands), the SIF-based results are a better fit than the TRENDY models, which do not assimilate SIF. By contrast, in other biomes (e.g., tropical biomes), several TRENDY models are a better fit than the SIF-based linear model. Note that the red box indicates the mean  $R^2$  value of the 15 TRENDY models and the vertical bar is the range of  $R^2$  values from the 15 models.

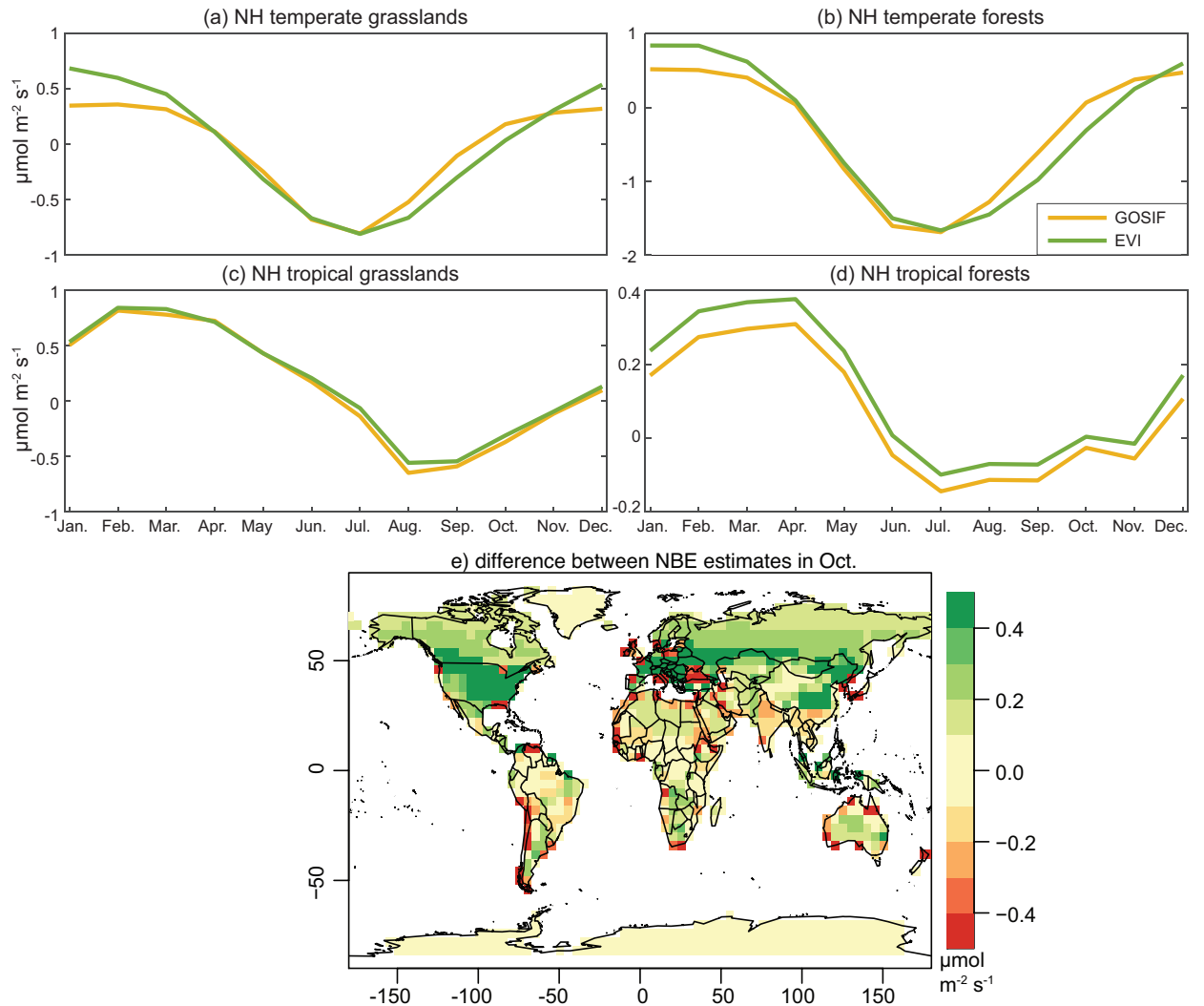


**Figure 4.** Estimated NBE from inverse modeling simulations that use GOSIF (yellow) and EVI (green) as predictor variables. Panels a-d compare the seasonal cycle. Inverse modeling simulations that incorporate GOSIF yield an different seasonal cycle in the extra-tropics relative to simulations using EVI (panels a and b). Specifically,  $\text{CO}_2$  uptake during northern hemisphere fall declines more quickly in the SIF simulations. By contrast, results for tropical biomes (panels c and d) show little difference between the two inverse modeling simulations. In addition, panel e compares spatial patterns in estimated NBE during October (i.e., GOSIF simulations minus EVI simulations), a month when the estimates yield different seasonal patterns across the northern extra-tropics. Green colors indicate greater  $\text{CO}_2$  uptake (or less  $\text{CO}_2$  release to the atmosphere) in simulations using EVI compared to those using GOSIF. Overall, panel e indicates broad differences between the NBE estimates across the northern extra-tropics.

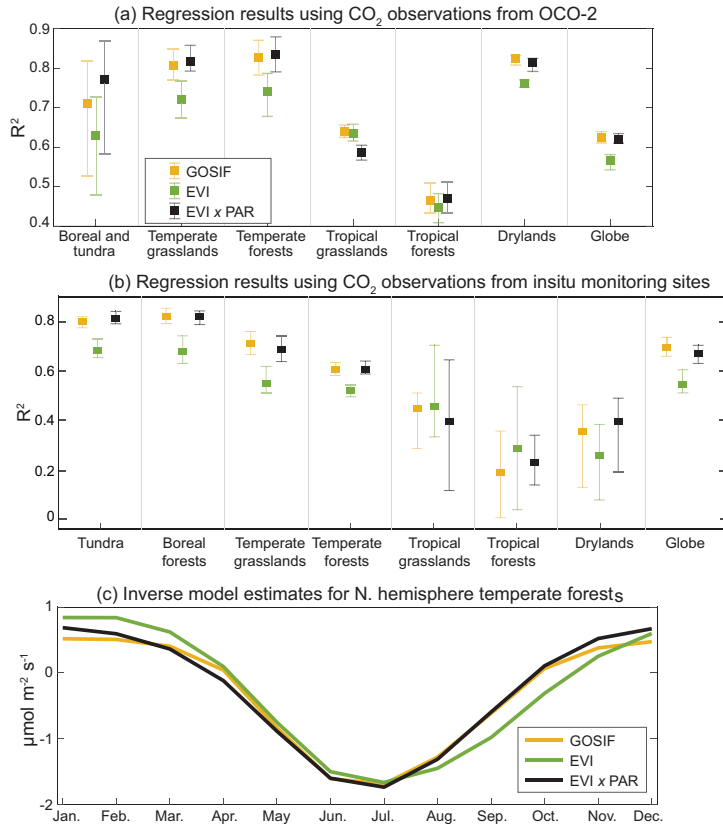


**Figure 5.** The fit ( $R^2$ ) against OCO-2 observations using a linear model of GOSIF, EVI, and  $\text{EVI} \times \text{PAR}$  as predictor variables. Panel (c) displays NBE estimated by the inverse model when using GOSIF, EVI and  $\text{EVI} \times \text{PAR}$  as predictor variables. Note that panels (a) and (c) assimilate CO<sub>2</sub> observations from OCO-2 while panel (b) shows the results of analysis using CO<sub>2</sub> observations from in situ CO<sub>2</sub> monitoring sites. Across all simulations, we find that EVI, when multiplied by PAR, is as skillful a predictor of NBE in the extra-tropics as SIF. Furthermore, NBE estimated in the inverse model using  $\text{EVI} \times \text{PAR}$  as a predictor variable exhibits a similar seasonal cycle as NBE estimated using GOSIF as a predictor.

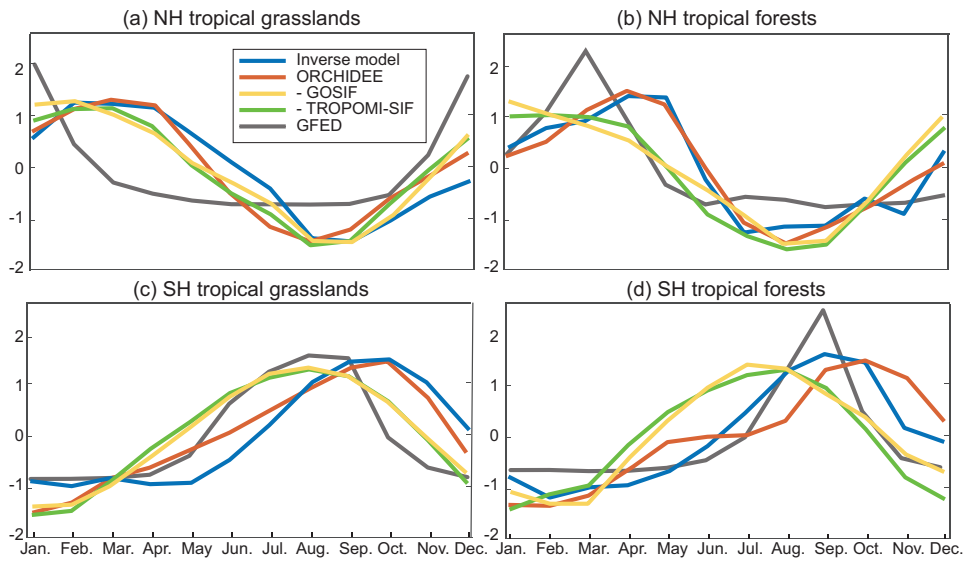


**Figure 6.** The seasonal cycle of NBE from the inverse model (blue), the ORCHIDEE model (red), GOSIF (yellow), TROPOMI-SIF (green), and GFED (charcoal) in different tropical biomes. Each product has been normalized to have a mean of zero and standard deviation of one for easier comparison. SIF in the tropics is out of phase with the seasonal cycle of the inverse modeling estimate and with ORCHIDEE, a bottom-up model that is more skillful at predicting CO<sub>2</sub> observations from OCO-2 relative to other TRENDY models.